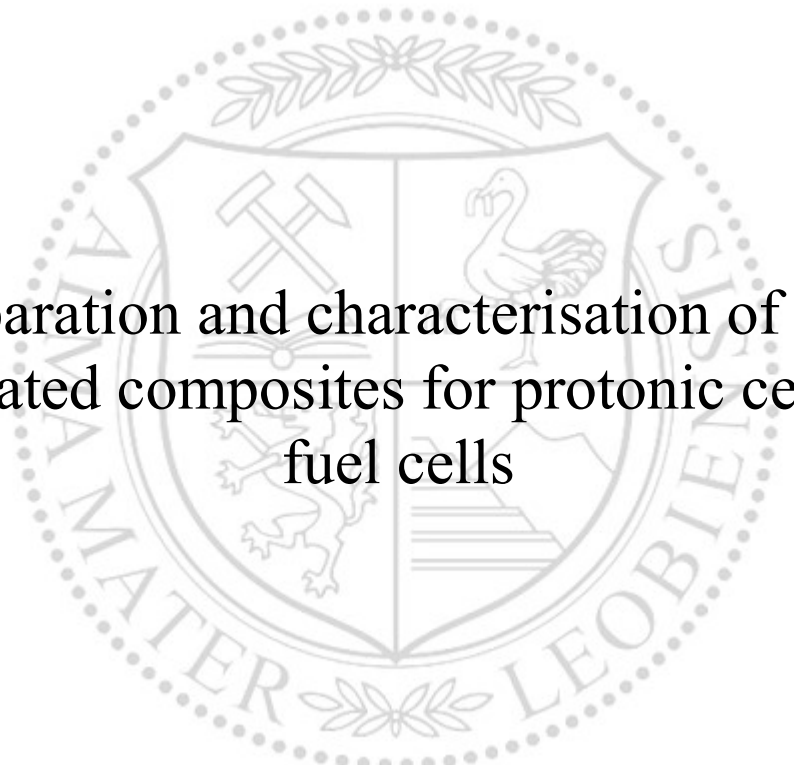Chair of Physical Chemistry

Master's Thesis

Preparation and characterisation of self-generated composites for protonic ceramic fuel cells

Christina Nader, BSc

May 2021

EIDESSTATTLICHE ERKLÄRUNG

Ich erkläre an Eides statt, dass ich diese Arbeit selbständig verfasst, andere als die angegebenen Quellen und Hilfsmittel nicht benutzt, und mich auch sonst keiner unerlaubten Hilfsmittel bedient habe.

Ich erkläre, dass ich die Richtlinien des Senats der Montanuniversität Leoben zu "Gute wissenschaftliche Praxis" gelesen, verstanden und befolgt habe.

Weiters erkläre ich, dass die elektronische und gedruckte Version der eingereichten wissenschaftlichen Abschlussarbeit formal und inhaltlich identisch sind.

Datum 06.05.2021

_____
Unterschrift Verfasser/in
Christina Nader

Acknowledgements

Kurzfassung

Herausforderungen wie die globale Erwärmung, die Umweltverschmutzung, der steigende Energiebedarf und die Endlichkeit der fossilen Brennstoffe stellen uns vor die Aufgabe, alternative erneuerbare Energiesysteme zu finden. Ein Aspekt ist die Effizienzsteigerung neuer Technologien, die noch nicht vollständig entwickelt sind. Brennstoffzellen und Elektrolysezellen sind ein vielversprechender Ansatz, da sie umweltfreundlich und kostengünstig sind und höhere Wirkungsgrade als herkömmliche verbrennungsbasierte Systeme ermöglichen. Diese Arbeit befasst sich mit protonischen keramischen Brennstoffzellen (PCFC), einer Art von Brennstoffzelle, die protonenleitende Oxide als Elektrolytmaterial verwendet. Ein Grund, warum diese Technologie noch keine breite Anwendung gefunden hat, ist die begrenzte Leistungsdichte von PCFCs. Die schlechte Sauerstoffreduktionsrate an der Kathode ist der Hauptgrund, warum die Leistung nicht die Erwartungen erreicht. Da die Leistung der Kathode von den Komponentenmaterialien abhängt, ist die Entwicklung innovativer Kathodenmaterialien mit optimierten Eigenschaften ein wichtiger Bestandteil der Verbesserung von PCFCs.

In dieser Arbeit werden drei verschiedene Komposite, hergestellt durch in-situ Phasenzersetzung, hinsichtlich ihrer Eigenschaften für den Einsatz als Kathodenmaterial untersucht. Die hergestellten Komposite basieren auf der Idee der dreifach leitenden Oxide (TCO), die Protonen, Sauerstoffionen und Elektronen gleichzeitig leiten können. Da es schwierig ist, diese Eigenschaften in nur einem Material zu vereinen, besteht unser Ansatz darin, ein Komposit zu schaffen, in dem zwei verschiedene Phasen zusammen diese Aufgabe erfüllen.

Der erste Teil dieser Arbeit befasst sich mit der Herstellung der Materialien mittels der "one-pot" Synthese, einer neuen Methode, die auf der in-situ Phasenzersetzung geeigneter Precursoren basiert. Der zweite Teil befasst sich mit der grundlegenden Charakterisierung der synthetisierten Komposite. Dazu werden strukturelle und chemische Analysen, sowie Untersuchungen der Masse- und Ladungstransporteigenschaften durchgeführt. Zu den angewandten Methoden gehören Röntgenbeugung (XRD), Rastertransmissionselektronen-mikroskopie (STEM) und energiedispersive Röntgenspektrometrie (EDX), elektrische Leitfähigkeitsmessungen nach der van der Pauw-Methode und Leitfähigkeitsrelaxations-messungen. Post-Test-Analysen mittels STEM-EDX werden eingesetzt, um detaillierte Einblicke in Effekte zu erhalten, die während der Messungen auftreten. Die Ergebnisse der vorliegenden Arbeit werden mit Literaturdaten verglichen.

Abstract

Challenges like global warming, environmental pollution, the increasing demand for energy and the finite nature of fossil fuels presents us with the challenge of finding alternative renewable energy systems. One aspect involves the improvement of energy conversion efficiency of new technologies that are not yet fully developed. Fuel cells and electrolyser cells are promising devices as they are environmentally friendly, cost-effective and allow higher efficiencies than conventional combustion-based systems. This work deals with protonic ceramic fuel cells (PCFC), a type of fuel cell that utilises proton-conducting oxides as electrolyte material. One reason why this technology has not yet found widespread application is the limited power density of PCFCs. The poor rate of oxygen reduction at the cathode is the main reason why the performance does not reach the expectations. As the performance of the cathode depends on component materials, the development of innovative cathode materials with optimised properties is an important part of the improvement of PCFCs.

In this thesis, three different composites, prepared by in-situ phase decomposition are investigated in terms of their properties for the application as cathode material. The composites produced are based on the idea of triple conducting oxides (TCO), which can conduct protons, oxygen-ions and electrons simultaneously. As it is difficult to combine these properties in just one material, our approach is to create a composite in which two different phases together fulfil this task.

The first part of this work deals with the preparation of the materials using the one-pot synthesis, a new method based on in-situ phase separation of suitable precursors. The second part addresses the fundamental characterisation of the synthesised composites. Therefore, structural and chemical analyses, as well as investigations of mass- and charge transport properties are carried out. The methods applied include X-ray diffraction (XRD), scanning transmission electron microscopy (STEM) and energy-dispersive X-ray spectrometry (EDX), electrical conductivity measurements by van der Pauw method and conductivity relaxation measurements. Post-test analyses by STEM-EDX are employed to obtain detailed insights into effects that occur during the measurements. The results of the present study are then compared with literature data.

Table of contents

1   Introduction

1.1   Motivation

Currently we have to face challenges like global warming, environmental pollution, the increasing demand for energy and the finite nature of fossil fuels. These aspects lead to a need and thus increased research in the field of new energy systems. In order to no longer be dependent on fossil resources and to reduce emissions, alternative renewable energy sources must be found. A further approach to cope with the current challenges is the improvement of energy conversion efficiency of new technologies that are not yet fully developed. Fuel cells and electrolyser cells are environmentally friendly, cost-effective and promising alternative power conversion devices. The chemical energy of hydrogen (or other fuels) is converted directly into electricity and thermal energy and vice versa. The major advantage of the fuel cell technology is that it is not limited by the Carnot efficiency. As a result, fuel cells can achieve higher efficiencies than conventional combustion-based systems. Further advantages are the conversion with zero emissions and the simple construction. Fuel cells have few to no moving parts, which means that there is no wear due to movement and the operation is comparatively quiet. Protonic ceramic fuel cells (PCFC) are a type of fuel cell that utilise proton-conducting oxides as electrolyte material. Compared to other types of fuel cells the electrolyte of PCFCs shows high ionic conductivity at intermediate temperatures (400 ≤ T/°C ≤ 600), which is preferable due to lower degradation of the materials at lower temperatures. However, their peak power density does not reach the values of traditional solid oxide fuel cells (SOFC), which utilise less conductive, oxygen-ion conducting electrolytes and are operated at higher temperatures (850 ≤ T/°C ≤ 1000°C). One limiting factor of the power density of PCFCs is the poor rate of oxygen reduction at the cathode. The performance of the cathode depends on component materials, which are currently mostly mixed oxide ion and electron conductors (MIEC) that are also used in SOFCs. [1–4]

1.2   Aim of this work

One approach to improvement of PCFCs is the development of innovative cathode materials with optimised properties. This thesis deals with the synthesis and characterisation of self-organised composites. The materials produced are based on the idea of triple conducting oxides (TCO), which are capable of conducting protons, oxygen-ions and electrons simultaneously. This property leads to an extension of the reaction area to the entire surface of the cathode material and thus to a possibly increased rate of oxygen reduction at the cathode. Since most materials can only conduct a maximum of two species well, it is difficult to combine these properties in just one material. Our approach is therefore to create a composite material in which two different phases together fulfil this task. The composites are synthesised using one-pot synthesis, a new method based on in-situ phase separation of

suitable precursors. The material forms two perovskite phases, where one has a good protonic conductivity and the other has a high catalytic activity for oxygen reduction and good electronic conductivity. For the fundamental characterisation of the synthesised materials, chemical analyses and electrochemical tests are carried out. The different characterisation methods include X-ray diffraction measurements, scanning transmission electron microscopy and energy-dispersive X-ray spectrometry analysis, electrical conductivity measurements by van der Pauw Method and conductivity relaxation measurements.

2 Fundamentals

2.1 Protonic ceramic fuel cell

The fundamental reaction in a fuel cell can be described by the combustion reaction between fuel and oxygen, in which energy is released in the form of heat. Depending on the choice of fuel, different reactions can take place. The product in the conversion of hydrogen is water.

Equation 1 | Reaction of hydrogen and oxygen

$$2\,H_2 + O_2 \rightleftharpoons 2\,H_2O$$
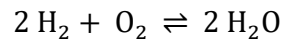
In a fuel cell, the reactants are separated from each other by a dense electrolyte that is electronically insulating and only allows the migration of certain ions [5]. Figure 1 shows the processes taking place during the operation of a fuel cell with a proton conducting electrolyte.
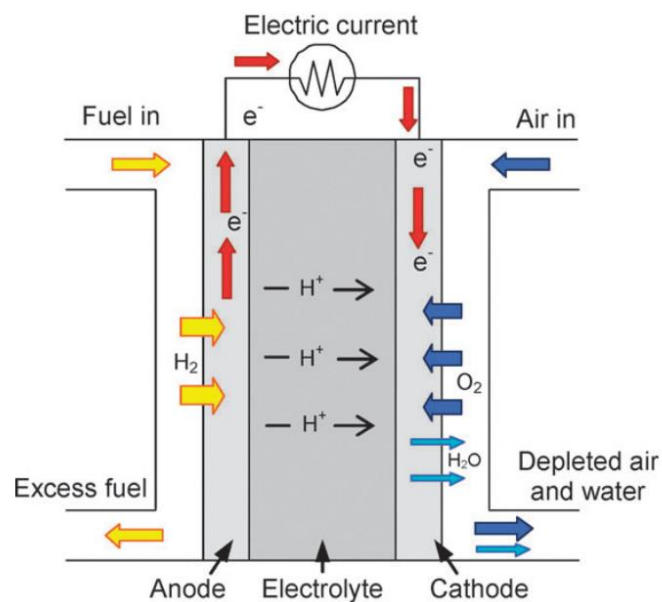

Figure 1 | Schematic diagram of the mode of operation of a PCFC [1]

The reactants hydrogen and oxygen are continuously delivered to the fuel cell. At the anode, hydrogen reacts by releasing electrons and thereby forming H^+ ions (protons). These H^+ ions pass through the electrolyte to the cathode, where they react with oxygen and electrons forming water. The electrons are transferred via an electrical circuit from the anode to the cathode, creating an electric current, which can supply an electrical consumer [5].

Equation 2 | Reaction at the anode

$$2\,H_2 \rightleftharpoons 4\,H^+ + 4\,e^-$$
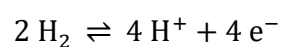
Equation 3 | Reaction at the cathode

$$O_2 + 4\,e^- + 4\,H^+ \rightleftharpoons 2\,H_2O$$
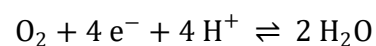
Due to the structure of a fuel cell, the electrochemical reaction produces electrical energy without being limited by the Carnot cycle. The use of fuel cells enables overall efficiencies greater than 80% in combined heat and power applications [6]. In contrast to low-temperature fuel cells like alkaline- or phosphoric acid fuel cells, solid oxide fuel cells (SOFCs) use a ceramic oxygen-ion conducting electrolyte. Due to the absence of a liquid electrolyte, the entire structure and the operation management becomes simpler [5]. Usually, this type of fuel cell is operated at high temperatures of 850 ≤ T/°C ≤ 1000. The reaction rate, which must be sufficiently fast, in order to make the converted energy usable, is accelerated at high temperatures. The reason for this is the increase in reaction kinetics, the higher electrochemical activity of the electrodes and the increased ionic conductivity of the electrolyte at higher temperatures. However, high operation temperatures also lead to some disadvantages. One reason why the SOFC has not yet found widespread application are the high costs of manufacturing and operation [6]. In the 1990s, it was recognised that for small systems, lowering the operation temperature leads to a reduction in costs [5]. Since then, efforts have been made to lower the operation temperature to 400 ≤ T/°C ≤ 600°C (intermediate temperature range, IT). Lower temperatures are less demanding on materials, so the choice of materials is expanded and the reliability of cell components like interconnectors and sealants is enhanced. This could lead to improved safety, lower degradation rates and reduced costs in several fields such as material preparation, cell fabrication and operation [2, 6]. In 2017 Dubois et al. estimate the costs for stack production of a PCFC that operates at 550°C, 27-37% lower than for a SOFC operating at 800°C [2, 7]. However, the reduction of the operation temperature leads to a decrease in power output through a lower activity of the electrodes and a decrease in ionic conductivity of oxygen-ion conducting electrolytes. In general, proton conduction in oxides exhibits lower activation energy (< 0.5 eV) than oxygen-ion conduction [7]. For this reason, the use of proton conducting oxides as electrolytes is a promising approach for high-performance fuel cells in the low temperature range.
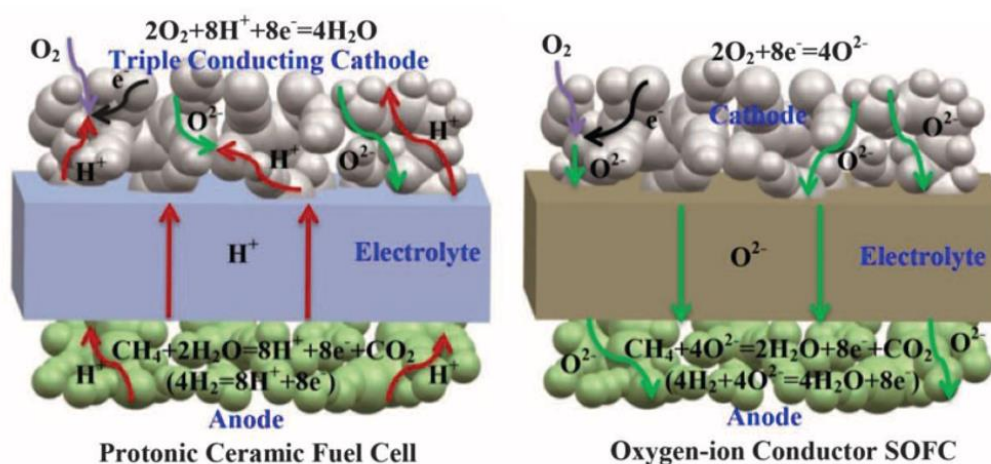

Figure 2 | Illustration of PCFC and SOFC operation [4]

In the late 1990s, Kreuer et al. demonstrated high proton conductivity and thermodynamic stability for acceptor-doped perovskite-type oxides. The observed proton conductivities for $BaZr_{1-x}Y_xO_{3-\delta}$ (BZY) (Y-dopant concentrations 15-20 mol%) were significantly higher than the oxygen-ion conductivities of the best oxygen-ion conductors below 700°C [8]. For PCFCs, fuel cells applying proton conducting electrolytes, a performance of 0.2-1.6 W cm^{-2} at 350 ≤ T/°C ≤ 600°C was predicted but the actual power output was not as high as expected [4]. The main issue is even today the absence of suitable cathodes, specially developed for operation in PCFCs at lower temperatures. At first, cathodes designed for traditional SOFCs operating at higher temperatures were utilised. The use of mixed ionic and electronic conducting materials (MIEC) limits the points at which the cathode reaction takes place to the contact areas of electrolyte and electrode, as illustrated in Figure 3a. One approach to increasing the number of active sites is the use of triple conducting oxides (TCO), shown in Figure 3b. Through the simultaneous conduction of protons, oxygen-ions and electrons, the entire cathode is electrochemically active. The result is a cathode with lower polarization resistance, leading to higher power densities [4].
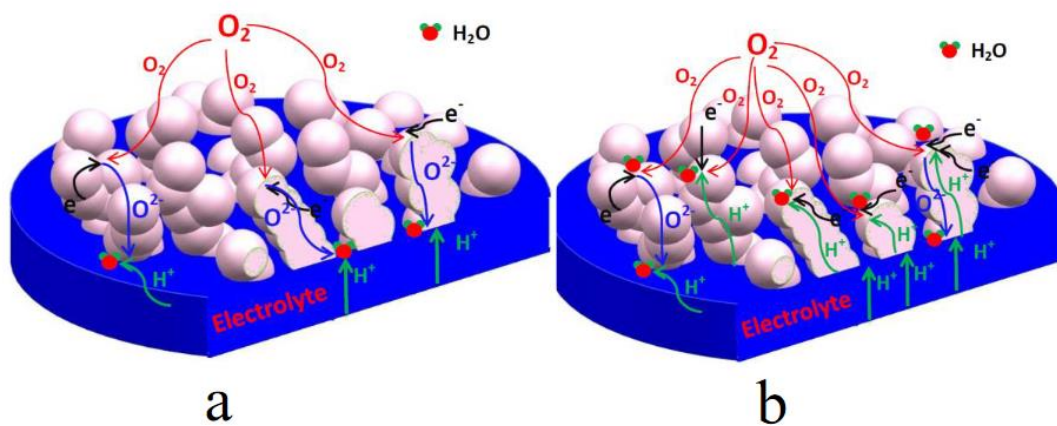

Figure 3 | Schematic diagram of the oxygen reduction mechanism with (a) a mixed ionic and electronic conducting (MIEC) cathode and (b) a triple conducting oxide (TCO) cathode [9]

Protonic ceramic fuel cells using triple conducting cathodes reportedly achieved a power density of 0.5 W cm^{-2} at 500°C operated with H_2 (utilising $BaZr_{0.4}Ce_{0.4}Y_{0.1}Yb_{0.1}O_3$ as electrolyte and $PrBa_{0.5}Sr_{0.5}Co_{1.5}Fe_{0.5}O_{5+\delta}$ as cathode material) [3]. Dubois et al. reported a power density of 0.156 W cm^{-2} at 500°C operated directly from methane fuel (anode-supported PCFC utilising $BaZr_{0.8}Y_{0.2}O_{3-\delta}$ (BZY20) as electrolyte, porous BZY20/Ni ceramic metal composite as anode and $BaCo_{0.4}Fe_{0.4}Zr_{0.1}Y_{0.1}O_{3-\delta}$ as cathode) [2]. An et al. reported peak power densities reaching 1.302 W cm^{-2} at 600°C and 0.535 W cm^{-2} at 500°C under a supply of humidified H_2 to the anode (anode supported PCFC utilising $BaCe_{0.55}Zr_{0.3}Y_{0.15}O_{3-\delta}$ (BCZY3) as electrolyte, NiO-BCZY3 composite as anode, and $Ba_{0.5}Sr_{0.5}Co_{0.8}Fe_{0.2}O_{3-\delta}$ (BSCF) as cathode). Furthermore, the electrical efficiency of PCFCs operated directly from hydrocarbon fuels reaches values of 55-65%, whereas the efficiency of SOFCs is 45-55% [7].

2.2 Material development

In 1981 Iwahara et al. reported high protonic conductivity for $SrCeO_3$-based perovskite (ABO_3) oxides in hydrogen-containing atmospheres at high temperatures [10]. Since then, a lot of research has been done in this field and the idea of triple conducting oxides (TCO) for application as cathode material evolved. TCOs are capable of conducting protons, oxygen-ions and electrons (holes) simultaneously ($H^+/O^{2-}/e^-/(h^\cdot)$). It is estimated that the protonic conductivity required to activate large parts of the cathode surface is 10^{-5} S cm^{-1} [11]. In oxides, hydrogen defects incorporated into the solid in the form of $OH_O^\cdot$ represent charge carriers for proton conduction. The proton uptake in oxides results from the equilibrium with defects (oxygen vacancies and electrons/holes) in the oxide lattice and depends on the concentration of these point defects [12]. Depending on the defect chemical regime, the incorporation of protons can take place via two different mechanisms. For electrolytes, the proton uptake occurs through water incorporation (acid-base reaction) [11, 13]. This mechanism is described by the following equation.

Equation 4 | Protonation of electrolytes

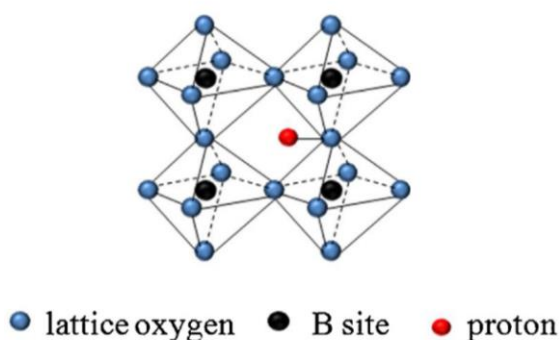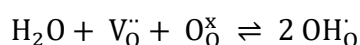$$H_2O + V_O^{\cdot\cdot} + O_O^x \rightleftharpoons 2\,OH_O^\cdot$$

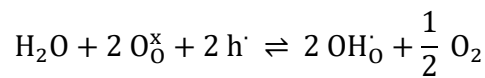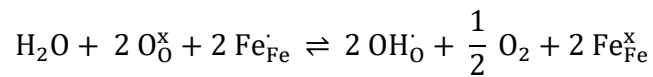*Figure 4 | Proton incorporated in a perovskite [14]*

$V_O^{\cdot\cdot}$ is an oxygen vacancy, O_O^x is a lattice oxygen and $OH_O^\cdot$ is a hydroxyl ion representing an interstitial proton associated with a lattice oxygen ion as illustrated in Figure 4. As can be derived from this equation, the existence of oxygen vacancies in a material is a prerequisite for the formation of protonic defects. Thus, an increasing concentration of oxygen vacancies leads to an increasing proton conductivity. However, considering perovskites to be used as cathode materials with mixed valent (redox-active) transition metal ions on the B-site, the situation is more complex [11]. Due to the ability of the transition metal to change valences (e.g. $Fe^{3+/4+}$), the following oxygen exchange equilibrium by redox reaction must be considered. In our case Fe_{Fe}^x represents the lower oxidation-state of iron Fe^{3+}, and $Fe_{Fe}^\cdot$ represents the higher one Fe^{4+}.

Equation 5 | Oxygen exchange equilibrium

$$\frac{1}{2}\,O_2 + V_O^{\cdot\cdot} + 2\,Fe_{Fe}^x \rightleftharpoons O_O^x + 2\,Fe_{Fe}^{\cdot}$$
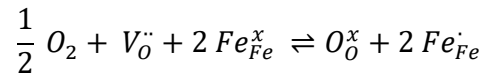
The combination of Equation 4 and 5 describes the second previously mentioned mechanism of proton incorporation in oxides, the proton uptake through proton incorporation (redox reaction) [11, 13]. Using $h^{\cdot}$, a p-type electronic defect (hole) to describe the high-oxidation-state cation $Fe_{Fe}^{\cdot}$, the equation describes the proton insertion reaction consuming holes. Thus, it is apparent that interactions between ionic and electronic defects are not to be neglected.

Equation 6 | Proton incorporation

$$H_2O + 2\,O_O^x + 2\,Fe_{Fe}^{\cdot} \rightleftharpoons 2\,OH_O^{\cdot} + \frac{1}{2}\,O_2 + 2\,Fe_{Fe}^x$$

$$H_2O + 2\,O_O^x + 2\,h^{\cdot} \rightleftharpoons 2\,OH_O^{\cdot} + \frac{1}{2}\,O_2$$

Since the combination of sufficient protonic and electronic conductivity in a single-phase material proves to be difficult, the approach of creating a dual-phase ceramic material by adding an electronic conducting phase was considered [14]. For barium cerate (BaCeO₃) based systems, different attempts have been carried out to improve the stability [15] or achieve both high protonic and electronic conductivity [16, 17]. The current work deals with composites consisting of (i) a primarily protonic conducting (PC) phase and (ii) a mixed ionic and electronic conducting (MIEC) phase to improve the performance of the material. Creating a stable and well performing composite requires sufficient chemical inertness and adequate percolation between the two phases. The common method for producing a composite is to prepare both single-phase oxides separately and mechanically mixing the crystallised powders. However, this method has a few disadvantages. Conventionally prepared composites result in micro sized grains, as shown in Figure 5.
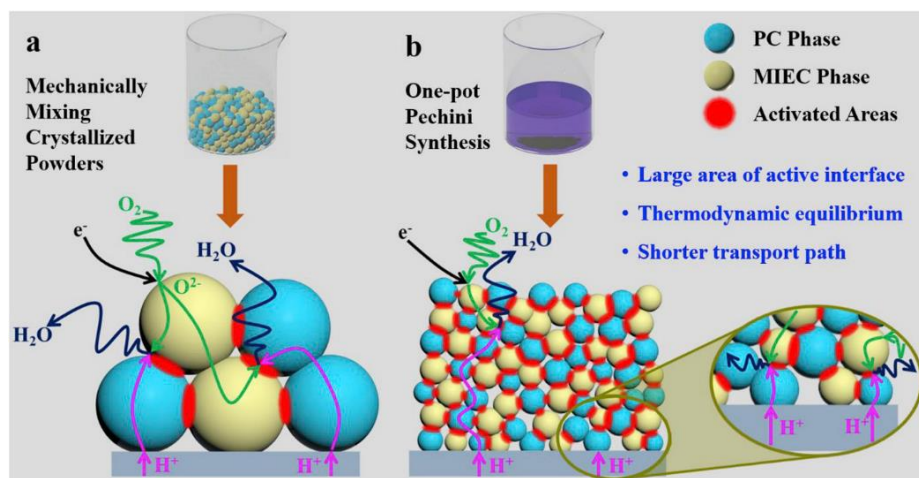

Figure 5 | Illustration of preparation, reactions and interface area of (a) microcomposite cathodes and (b) twin-perovskite nanocomposite cathodes [17]

This leads to the formation of "islands" of each phase and therefore to a poor two-phase percolation [14]. Thus, the transport paths for charged species are extended and the area of active interface is reduced in comparison to nanocomposites. Furthermore, the material is not in thermodynamic equilibrium, which can lead to cation interdiffusion. Sintering at high temperatures accelerates solid state reactions and results in the formation of undesired phases and interface impurities which leads to performance degradation [14, 17]. In 2016 Cheng et al. used a novel method, the so-called "one-pot" synthesis, for the preparation of stable and well-percolated self-generated composites [18]. This preparation method is less complex, and it produces very fine and homogenous powders. The composite is synthesised by EDTA-citric acid method and forms two thermodynamically stable phases by separation of a ceramic precursor [18, 19]. Among other perovskite-type oxides, the $BaCeO_3$ based system shows the highest proton conductivity, which is why it was also selected for the current work based on results from [12]. The ceramic precursor $BaCe_{0.5}Fe_{0.5}O_{3-\delta}$ (BCF55) decomposes during the calcination process at 1000°C into the Ce-rich oxide $BaCe_{0.85}Fe_{0.15}O_{3-\delta}$ (BCF8515) with orthorhombic crystal structure and the Fe-rich oxide $BaCe_{0.15}Fe_{0.85}O_{3-\delta}$ (BCF1585) with cubic crystal structure. The reason for the decomposition of the $BaCeO_3$-$BaFeO_x$ system (A^{II}:B^{IV} perovskite) into two thermodynamically stable phases, is the difference in the radii of the B-site elements of the perovskite [18]. Cerium, Ce^{4+} (VI) (0.87 Å) is much bigger than iron in both oxidation states Fe^{3+} (VI) (HS) (0.645 Å) and Fe^{4+} (VI) (0.585 Å) [20]. Both phases contain the same chemical elements in different concentrations and conduct protons and electrons simultaneously [18]. As shown in Figure 6, the Ce-rich phase BCF8515 mainly conducts protons, whereas the Fe-rich phase BCF1585 is the main electronic conductor. In addition, it was discovered that the BCF8515-BCF1585 composite exhibits also oxygen ion conductivity. Therefore, a triple conducting mixture of oxides is obtained, which is suitable for application as a cathode for PCFCs. Due to the limited solubility of ions in each phase, the composite is in thermodynamic equilibrium and neither cation diffusion between the phases, nor formation of secondary phases occur [18].
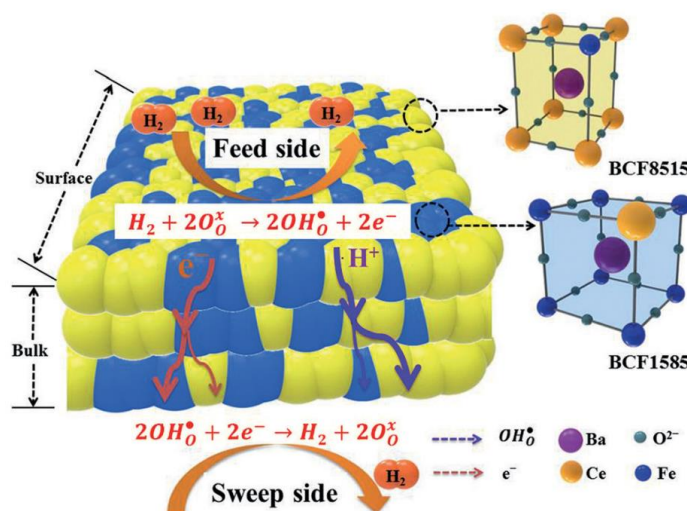

Figure 6 | Concept of dual-phase mixed protonic and electronic conduction using a membrane as an example [18]

2.3 Influence of chemical composition

The chemical formula of perovskites is ABO_3, where A and B represent two or more different cations. The cations on the A-site are usually large and 12-coordinate, whereas B-site cations are commonly small and 6-coordinate. Concerning the charge of the cations, different combinations are possible, e.g. $A^I:B^V$, $A^{II}:B^{IV}$ or $A^{III}:B^{III}$ [21]. This work focuses on $A^{II}:B^{IV}$ perovskites. The ideal perovskite structure is cubic, as illustrated in Figure 7. Positions highlighted in yellow represent the A-site cations, the red ones represent the B-site cations, and the green ones represent the lattice oxygen. Most perovskites do not crystallise in the ideal cubic crystal structure but are distorted and assume lower symmetries. For perovskites, a wide range of different chemical compositions is known, leading to a variety of different properties [21].
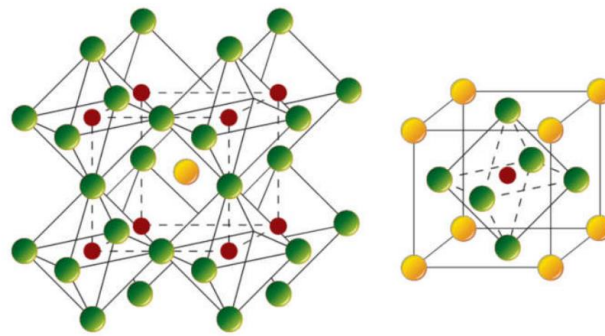

Figure 7 | Ideal cubic perovskite structure [22]

In this work, $BaCeO_3$ based perovskites are modified in terms of chemical composition and electrical conductivity. Barium occupies the A-site and cerium the B-site. By adding selected cations on the A- or B-site, the structure and the properties can be influenced. The perovskite structure tolerates certain differences in size or valence of the substituent ions. According to the kind of inserted ion the substitution leads to various kinds of defects in the structure [21]. Defects like e.g., oxygen ion vacancies enable the mobility of different ions, which is why they are desirable. However, a straightforward prognosis of the impact of certain dopants on the electrical conductivity is difficult, as the effects may be complex. There is no systematic or universal correlation between dopant ion and electrical conductivity [14]. Cheng et al. reported a decomposition for Fe-doped $BaCeO_3$ into a Ce-rich and an Fe-rich phase [18]. Partial substitution of the B-site with the multivalent (redox-active) transition metal Fe leads to p-type electronic defects (holes) that are largely localised on the Fe ions [11]. This enables electron transport from a low-oxidation-state cation to a high-oxidation-state cation in its vicinity ("small polaron mechanism") [23]. Thus the presence of Fe on the B-site leads to electronic conductivity and catalytic activity [11]. The partial substitution of $BaCe_{1-x}M_xO_{3-\delta}$ with trivalent redox-inactive cations (M = Y, Tm, Yb, Lu, In or Sc [14]) results in the formation of oxygen vacancies to maintain the electrical neutrality of the crystal.

In the chemical formula, δ indicates the number of oxygen ion vacancies per formula unit. The existence of these defects enables the conduction of oxygen ions through the crystal. In dry air, oxygen ions migrate by vacancy hopping from their original site to an adjacent vacant site [21]. In the presence of water, the formation of $OH_O^{\cdot}$ by incorporation of water into oxygen vacancies leads to protonic conductivity according to Equation 4. It was discovered that a large unit cell volume and distortions from the ideal lattice structure are beneficial to proton mobility and therefore result in higher protonic conductivity [14, 24]. This fits with Liu et al. reporting higher ionic conductivity with increasing ionic radii of the dopants [25]. The larger ionic radius leads to increased lattice distortion and high free volume. This enhances the ion diffusion and results in higher ionic conductivity. Furthermore, the material basicity has a significant impact on the proton uptake. Cations with low electronegativity leading to higher basicity of the material showed a positive effect on proton uptake [11]. However, high basicity also leads to lower stability against acidic gases like CO_2, which may be cause for degradation but is not discussed further in this work [18]. In summary, $BaCe_{1-x}M_xO_{3-\delta}$ substituted with trivalent cations shows increasing conductivity with increasing ionic radius and decreasing electronegativity of the dopant [14]. Yttrium Y^{3+} (VI) has a large ionic radius (0.900 Å [20]) compared to other trivalent cations (e.g. Sc^{3+} (VI) (0.745 Å), Lu^{3+} (VI) (0.861 Å), In^{3+} (VI) (0.800 Å) [20]) and possesses a low electronegativity. For $BaCeO_3$ based perovskites partial substitution with Y on the B-site leads to enhanced concentration of oxygen vacancies and shows the highest conductivity [14].

2.4 Methodology

This chapter provides concise descriptions of the analysis methods used. In addition to the methods listed, other measurements were also carried out. The results of these are also discussed later. However, these measurements were done by project partners, which is why the methods are not described in detail in this chapter.

2.4.1 One-pot synthesis

The one-pot synthesis uses the EDTA-citric acid method, a sol-gel process for the preparation of ceramics by inorganic polymerisation [26]. A great advantage of this method is its ease of use, as the reaction is less aggressive and the preparation is faster with higher outputs compared to the glycine-nitrate combustion synthesis. The sol-gel process includes four key steps. At the beginning, a colloidal suspension is formed by dissolving stoichiometric amounts of the precursors. The addition of an acid or a base catalyst to the precursor solution leads to cross-linking of particles. This step promotes polymerisation and is called sol to gel transition (gelation). In detail, hydrolysis and polycondensation reactions take place. During the aging process, there is stronger cross-linking, which leads to increasing viscosity and mechanical strength of the gel. The last step is the drying of the aged gel. There are several methods for extracting the solvent from the pores of the gel, which lead to different properties of the material. These include evaporation (xerogel), supercritical drying (aerogel), sublimation (lyogel) and freeze drying (cryogel) [27]. The procedure of the sol-gel process is illustrated in Figure 8. In this work, evaporation was used as the drying method. The powder produced is then calcined at 1000°C. During this step, the phase separation into the two thermodynamically stable phases occurs.
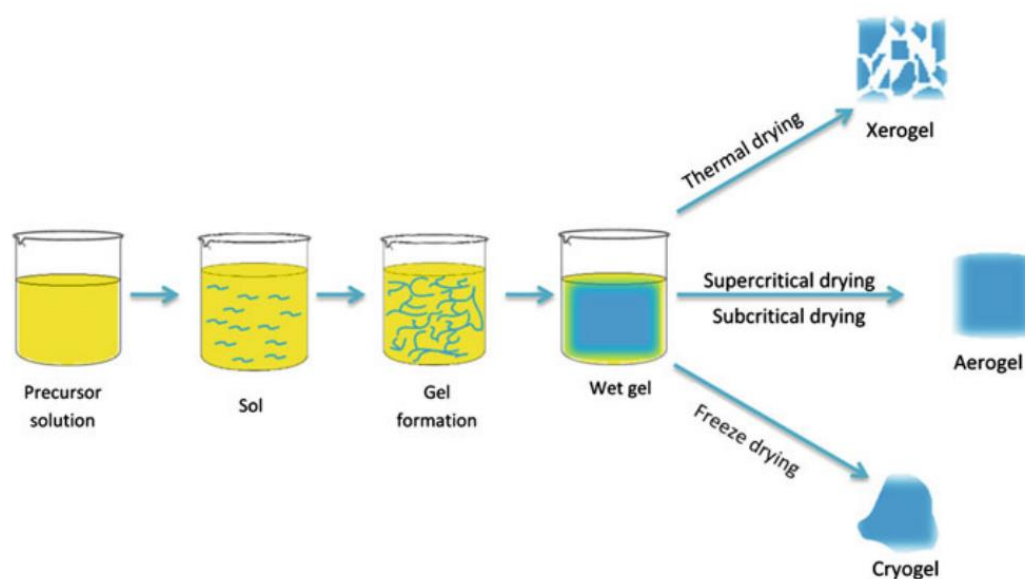

Figure 8 | Illustration of the sol-gel process [27]

2.4.2 Electrical conductivity measurements

In this work, the electrical conductivity (EC) is measured by the 4-point dc van der Pauw method. It is a technique for determining the specific resistivity (conductivity) and the Hall effect of thin, flat and dense sintered samples of arbitrary shape. Unlike the measurement method for bar-shaped samples, the electric current distribution of the sample need not be known, if certain conditions are met. The sample has to be homogenous in thickness and dense, i.e., it has no isolated holes. Furthermore the contacts must be sufficiently small and be placed at the circumference of the sample [28]. The four contacts A, B, C and D are placed on the sample as shown in Figure 9. To measure the specific resistance a current is applied at contact A and taken off at contact B, and the potential difference V_D-V_C is measured between the contacts D and C. The resistance $R_{AB,CD}$ is defined in Equation 7. Analogously, to define the resistance $R_{BC,DA}$, a current is applied at the contact B and taken off at the contact C, and the potential difference V_A-V_D is measured between the contacts A and D [28].
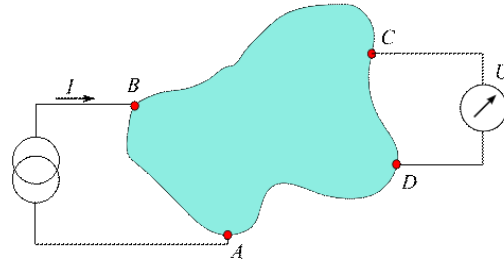
Figure 9 | Illustration of the measurement configuration for the van der Pauw method [29]

Equation 7 | Formula for the determination of $R_{AB,CD}$

$$R_{AB,CD} = \frac{U_{CD}}{I_{AB}}$$

Equation 8 | Formula for the determination of $R_{BC,DA}$

$$R_{BC,DA} = \frac{U_{DA}}{I_{BC}}$$

Equation 9 | Formula for the determination of the specific resistance [28]

$$\exp(-\pi \cdot R_{AB,CD} \cdot \frac{d}{\varrho}) + \exp(-\pi \cdot R_{BC,DA} \cdot \frac{d}{\varrho}) = 1$$

Equation 10 | Formula for the specific conductivity

$$\sigma = \frac{1}{\varrho}$$

The van der Pauw method uses the existing relation between $R_{AB,CD}$ and $R_{BC,DA}$ to obtain the specific resistance ϱ of the material [30]. If the thickness d of the sample and the resistances are known, the specific resistance can be calculated by using Equation 9. The reciprocal of the specific resistance is the specific conductivity σ, as shown in Equation 10.

2.4.3 Conductivity relaxation measurements

The dc-conductivity relaxation (CR) technique is used to determine the oxygen exchange kinetics. Materials with properties changing with the oxygen partial pressure are suitable for applying relaxation techniques like e.g., conductivity relaxation utilised in this work. Oxygen-deficient materials, as studied in this work, respond to a step-wise change in oxygen partial pressure by incorporating or releasing oxygen until a new equilibrium is reached [31]. The change in oxygen partial pressure leading to a change in the concentration of charge carriers results in a change in electrical conductivity [32]. To determine the kinetic parameters for oxygen exchange from the data received, the material has to show predominantly electronic conductivity. If the electronic conductivity is significantly higher than the ionic conductivity, the time for the change throughout the material is almost exclusively controlled by the movement of ionic species [32]. The sample in van der Pauw geometry undergoes a change in pO_2 while applying a constant current to the sample and measuring the voltage. With this data, the conductivity σ_t for each time step can be determined. The normalized specific conductivity is calculated using Equation 11, where σ_0 is the conductivity before the pO_2 change and σ_∞ is the conductivity after the pO_2 change at an equilibrated state. σ_t is the conductivity at a certain time during the relaxation. With this information, the change in normalized specific conductivity $\bar{\sigma}_t$ (sigma(norm)) is plotted as a function of time, resulting in the relaxation curve of the oxidation or reduction [33].

Equation 11 | Formula for the normalised specific conductivity [33]

$$\bar{\sigma}_t = \frac{\sigma_t - \sigma_0}{\sigma_\infty - \sigma_0}$$

The oxygen exchange kinetics is determined by the chemical bulk diffusion coefficient D_{chem} and the chemical surface exchange coefficient k_{chem}. These parameters can be obtained from nonlinear least squares fits of the solution of the suitable diffusion equation to the conductivity relaxation data [34]. Depending on the kinetic regime, different fitting functions are adequate for describing the relaxation curves. Equation 12 assumes that the oxygen exchange kinetics is rate-limited by the surface exchange (incorporation or release) of oxygen, giving a value for k_{chem}. This is the case if the ordinate intercept of the $ln(1-\sigma_{norm})$ vs. t plot is around 0. If the ordinate intercept is around −0.21, the process is bulk diffusion-limited and therefore Equation 13 is applied. Equation 14 includes both processes and is only applied when the fits of only D_{chem} and k_{chem} do not fit the relaxation curves [33]. In this case the ordinate intercept is between −0.21 and 0.

Equation 12 | Formula for k_{chem} controlled kinetics [33]

$$\ln(1 - \sigma_{norm}) = -\frac{2 \cdot k_{chem}}{L} \cdot t$$

Equation 13 | Formula for D_{chem} controlled kinetics [33]

$$\ln(1 - \sigma_{norm}) = \ln\left(\frac{8}{\pi^2}\right) - \frac{D_{chem} \cdot \pi^2}{L^2} \cdot t$$

Equation 14 | Formula for mixed controlled kinetics [33]

$$\ln(1 - \sigma_{norm}) = \ln\left(\frac{2 \cdot k_{chem}^2}{D_{chem}^2 \cdot \gamma^2 \cdot \left(\frac{k_{chem} \cdot L}{D_{chem}}\right)^2 + \frac{\gamma^2 \cdot L^2}{4} + \frac{k_{chem} \cdot L}{2 \cdot D_{chem}}}\right) - D_{chem} \cdot \gamma^2 \cdot t$$

L is the thickness of the sample and γ is the Eigenvalue defined as $\gamma \cdot \tan\left(\frac{\gamma \cdot L}{2}\right) = \frac{k_{chem}}{D_{chem}}$ [33]. The solutions are found by iteration (usually 8-12 iteration steps [31]) and can be used to determine D_{chem} and k_{chem}. For the solution of the diffusion equations two general assumptions are made: (i) D_{chem} and k_{chem} are considered to be constant during the pO_2 step and (ii) first-order kinetics is assumed for the oxygen exchange reaction [34]. These assumptions are only met if the changes in oxygen partial pressure are sufficiently small. At the same time, the change in pO_2 should not be *too* small, since the noise of the electrical conductivity should not obscure the signal [34]. Therefore, a compromise has to be found.

3   Experimental

3.1   Sample preparation

A series of BaCe$_{0.8-x}$Fe$_x$Y$_{0.2}$O$_{3-\delta}$ (0.2≤x≤0.6) samples are prepared by one-pot synthesis using the EDTA-citric acid method. The selection of samples is shown in Table 1. All samples contain 20% yttrium on the B-site. The amount of iron was chosen in the range of 20-60% to obtain self-generated composites, since Fe contents below 0.15 or above 0.8 lead to single phase materials, as shown in Figure 10 [18].
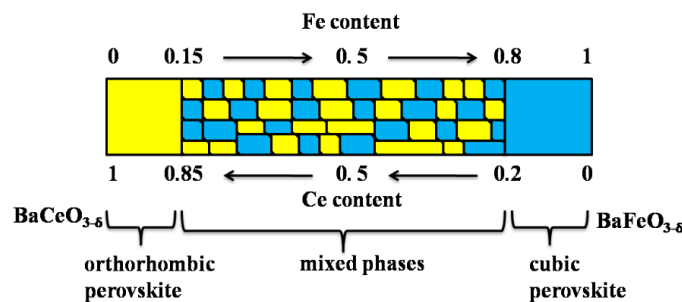
Figure 10 | Schematic phase diagram of the dual-phase BaCe$_{1-x}$Fe$_x$O$_{3-\delta}$ oxide system [19]

Table 1 | Self-generated composites investigated in this work

	Abbreviation	Fe concentration [%]	Ce concentration [%]
BaCe$_{0.2}$Fe$_{0.6}$Y$_{0.2}$O$_{3-\delta}$	BCFY262	60	20
BaCe$_{0.4}$Fe$_{0.4}$Y$_{0.2}$O$_{3-\delta}$	BCFY442	40	40
BaCe$_{0.6}$Fe$_{0.2}$Y$_{0.2}$O$_{3-\delta}$	BCFY622	20	60

3.1.1   Synthesis and structure analysis

Stoichiometric amounts of the metal nitrates Ba(NO$_3$)$_2$, Ce(NO$_3$)$_3$·6H$_2$O, Fe(NO$_3$)$_3$·9H$_2$O and Y(NO$_3$)$_2$·6H$_2$O are dissolved in distilled water in a stainless steel vessel. All chemicals are obtained from Sigma Aldrich with analytical grade quality. The solution is heated to approximately 70°C and mixed continuously with a magnetic stirrer. Having the metal nitrates completely dissolved, one mole per mole cations of anhydrous citric acid and EDTA (ethylenediaminetetraacetate) is added to the solution. By adding 25% aqueous NH$_3$ solution, the pH value is adjusted to about 8 and the previously cloudy solution becomes clear. Subsequently, the temperature is slowly raised up to 500°C to evaporate the water and form a gel. When the gel is sufficiently dry, it self-ignites and combusts. Afterwards, the raw ash is carefully crushed in a porcelain mortar and filled into an aluminium oxide crucible. The calcination of the powder is carried out in a chamber furnace from Carbolite for 10 h in air leading to the separation into two thermodynamically stable phases. Table 2 shows the temperature program for the calcination process.

Table 2 | Temperature program for the calcination process

Heating rate	5 K min^{-1}
Dwell time	10 h
Cooling rate	5 K min^{-1}

To determine the phase composition, the calcined powder is analysed by X-ray powder diffraction (XRD) using the diffractometer BRUKER-AXS D8 Advance ECO. The measurement is performed at room temperature using a Cu Kα radiation source operated at 40 kV and 25 mA (1000 W) with a scanning rate of 0.01°s^{-1}. XRD measurements were carried out by Christian Berger at Montanuniversitaet Leoben. Further investigations of the material structure are performed by STEM analysis with a TITAN^{3} G2 60-300. The sample preparation is carried out on a focused ion beam (FIB) microscope FEI NOVA 200 Nanolab. STEM analyses were conducted by Judith Lammer at Centre for Electron Microscopy Graz.

3.1.2   Sintering and sample contacting

For further tests, i.e. electrical conductivity and conductivity relaxation measurements, dense (above 95% relative density [33]) and fine polished samples are required. As it was not possible to achieve these properties with conventional pressing and sintering, spark plasma sintering (SPS) was considered. The milling and sintering process was carried out at Max Planck Institute for Solid State Research (Stuttgart, Germany). As wet ball milling leads to decomposition into $BaCeO_3$, $BaCO_3$ and Fe_3O_4, the calcined powder is ground in a dry ball mill to achieve a suitable particle size distribution for further processing. For BCFY442, 5 min at 1000°C was chosen as the SPS standard parameter resulting in 100% relative density. The dense samples from SPS are cut to size with a diamond saw. As shown in Figure 11a, the sample is square with a cross section of approximately 5x5 mm² and a thickness of about 1 mm. The surface of the sample is polished with a manual water-cooled polisher to a fineness of 1 μm. Similar to Figure 11b, four small contacts are placed in van der Pauw geometry on the sample. Finally, the sample is connected to a sample holder, as shown in Figure 11c, and placed into a quartz glass reactor. Table 3 displays the thicknesses of the samples. The relative densities of the samples are estimated to be 93-95%.

Table 3 | Sample thicknesses for EC and CR measurements

	Sample thickness [μm]
$BaCe_{0.2}Fe_{0.6}Y_{0.2}O_{3-\delta}$	923
$BaCe_{0.4}Fe_{0.4}Y_{0.2}O_{3-\delta}$	1085
$BaCe_{0.6}Fe_{0.2}Y_{0.2}O_{3-\delta}$	896

A   B

D   b   C

a   c
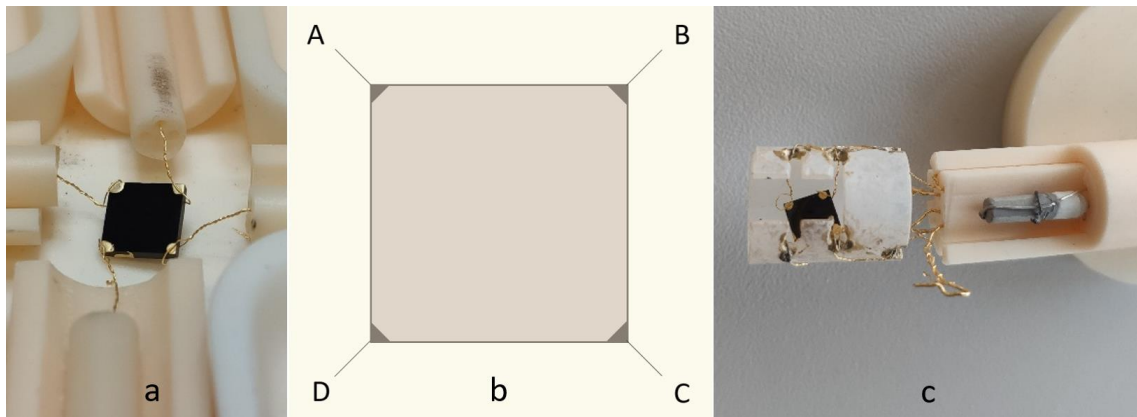
Figure 11 | Sample with contacts in van der Pauw geometry

3.2 Electrical conductivity measurements

The electrical conductivity measurements are carried out in a quartz glass reactor as shown in Figure 12a, placed into an oven and connected to the gas supply (gas mixtures of O_2 and Ar). For the application of the current and the measurement of the sample voltage, a source meter and a nano-voltmeter are connected to the contacts of the sample. Two different setups were used for the characterisation of the samples. Setup I consists of a Keithley 2400 SourceMeter and a Keithley 182 SENSITIVE DIGITAL VOLTMETER. Setup II uses a Keithley 2400 SourceMeter and a Keithley 2182A NANOVOLTMETER. An illustration of the setup is shown in Figure 12b. The sample parameters and used setups are summarised in Table 4.
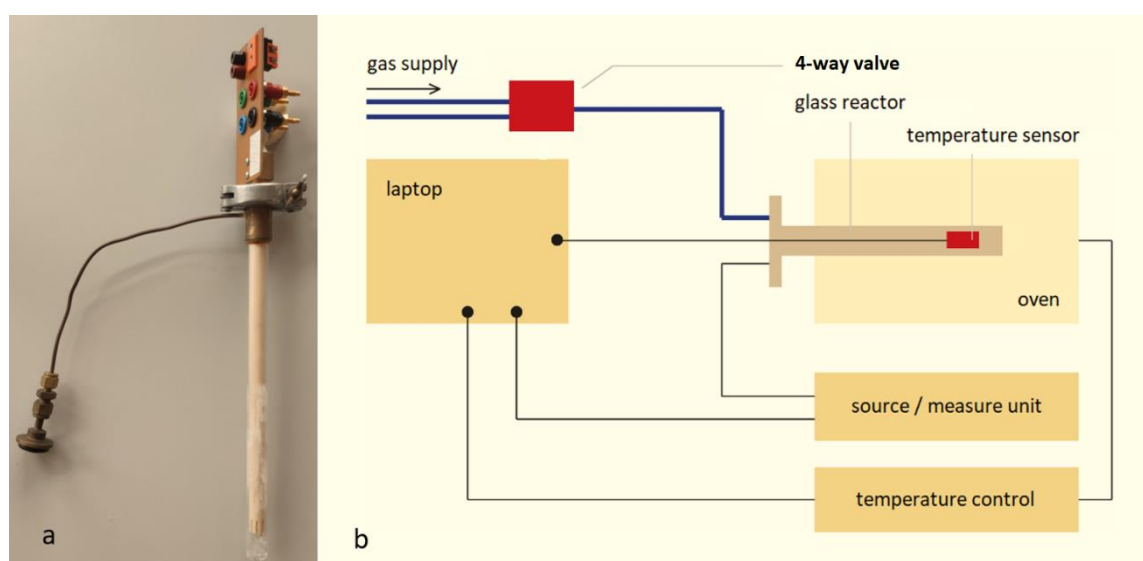
Figure 12 | (a) Quartz glass reactor for EC and CR measurements and (b) illustration of the setup

Table 4 | Setup assignment for all samples

	Setup
$BaCe_{0.2}Fe_{0.6}Y_{0.2}O_{3-\delta}$	I
$BaCe_{0.4}Fe_{0.4}Y_{0.2}O_{3-\delta}$	I
$BaCe_{0.6}Fe_{0.2}Y_{0.2}O_{3-\delta}$	II

The EC measurements are carried out in a temperature range of $400 \leq T/°C \leq 800$ in dry O_2-Ar atmosphere. After 10 days equilibrating in humidified O_2-Ar atmosphere (75% relative humidity, where 100% corresponds to the equilibrium water vapour pressure at 25°C), measurements at $400 \leq T/°C \leq 600$ are conducted. This temperature range is selected in order to prevent Si-poisoning occurring at high temperatures in humid atmosphere [35]. After another 10 days of equilibrating in dry O_2-Ar atmosphere, measurements in the same temperature range as before are carried out to check reversibility/reproducibility.

For each temperature, at an interval of 50°C, the electrical conductivity is measured at different oxygen partial pressures, i.e. 1.0×10^{-1} bar pO_2 and 1.5×10^{-1} bar pO_2. The applied current depends on the sample and the temperature. It is selected to obtain probe voltages in the range of 7-9 mV. For BCFY442 the applied current is typically in the range of $20 \leq I/\mu A \leq 120$. As the specific resistance of BCFY622 is higher compared to BCFY442, the applied current is lower – in a range of $2 \leq I/\mu A \leq 30$. For BCFY262 the applied current is typically in the range of $130 \leq I/\mu A \leq 300$. The current profile is shown in Figure 13. During the first half of the measurement (15 min), the resistance $R_{AB,CD}$ is determined, whereas in the second half, the resistance $R_{BC,DA}$ is measured. According to Equation 10, the specific conductivity is calculated from $R_{AB,CD}$, $R_{BC,DA}$ and the sample thickness d.
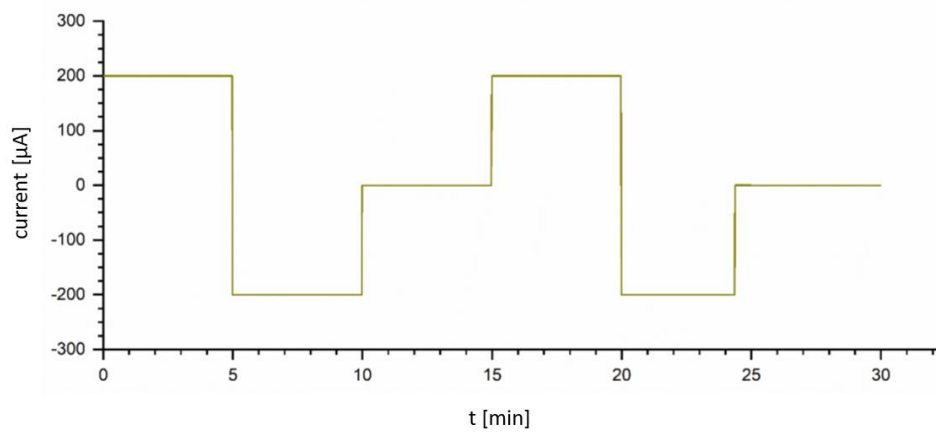
Figure 13 | Current profile during a measuring process

3.3   Conductivity relaxation measurements

The conductivity relaxation measurements are carried out within the same setups used for the electrical conductivity measurements with van der Pauw method. Similar to the EC measurements, the data is collected in 50°C steps in dry and humid atmosphere. The equilibrated sample undergoes a small step-wise change in oxygen partial pressure (1.0×10^{-1} ≤ pO_2/bar ≤ 1.5×10^{-1}) which causes a change in resistance and therefore in the conductivity of the sample, as shown in Figure 14. For all temperatures in dry and humid atmosphere, measurements in oxidising and reducing direction are carried out.
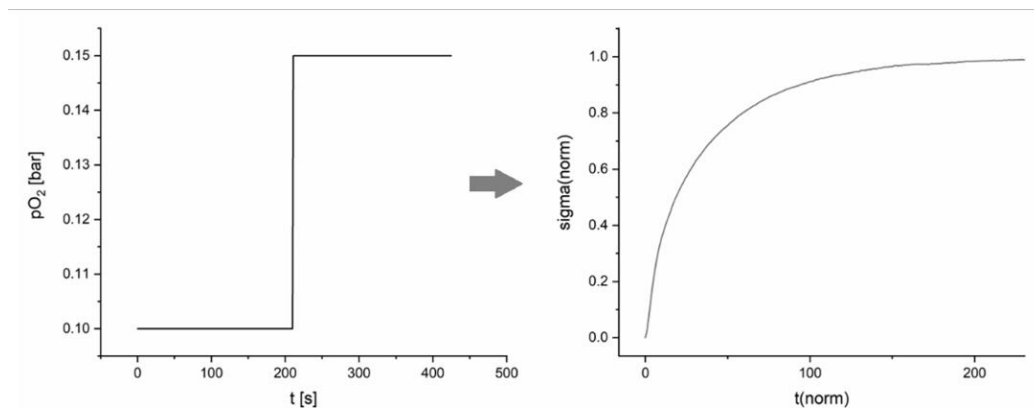
Figure 14 | Ideal pO₂ change and the resulting relaxation curve of BCFY262 at 700°C

D_{chem} and k_{chem} are obtained by executing the fitting procedure of the relaxation curve according to Equation 12, 13 and 14. Usually 20 iteration steps are sufficient for each equation. Figure 15 shows the conductivity relaxation curve for the oxidation of BCFY262 at 700°C. The model assuming bulk diffusion-controlled kinetics fits the curve best in this case.
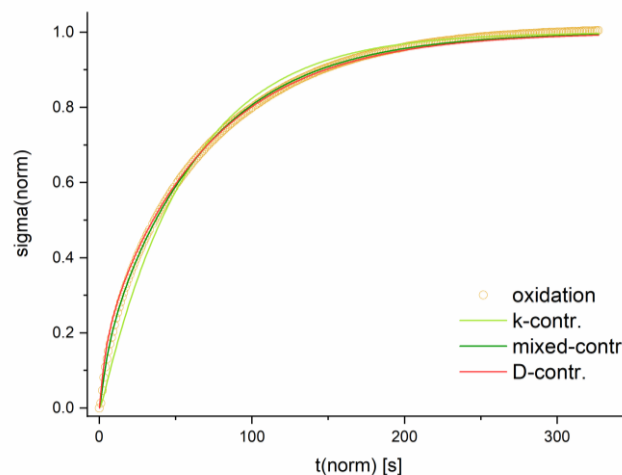
Figure 15 | Conductivity relaxation curve for the oxidation process of BCFY262 at 700°C and fits for different kinetic regimes

For the conductivity relaxation measurement, the setting of the gas supply is particularly important. The gas flow has to be high enough to ensure that the change in oxygen partial pressure takes place within a very short time. This needs to be ensured as the diffusion equations assume an instantaneous change in pO_2. If the gas flow is too low, resulting in a slow change in pO_2, the relaxation profile is distorted (longer than expected) [32]. Thus, the kinetic parameters are underestimated, as the oxygen exchange is neither dominated by the incorporation of oxygen on the surface of the material, nor by bulk diffusion, but rather (partially or completely) by the gas flow. In our case, a total constant gas flow of 2.5 dm^3 h^{-1} is applied in setup I and 2.0 dm^3 h^{-1} in setup II. With some other perovskite materials, the oxidation process occurs faster than the corresponding reduction process [32, 36]. This is also the case for BCFY262 as shown in Figure 16. For the oxidation of BCFY262, the first data received, deviated from the expected result due to insufficient gas flow. In contrast to the measurements in reducing direction, the tests in oxidising direction did not show bulk diffusion-controlled kinetics. After increasing the total gas flow to 2.5 dm^3 h^{-1}, diffusion-controlled kinetics was also observed for the oxidation process.
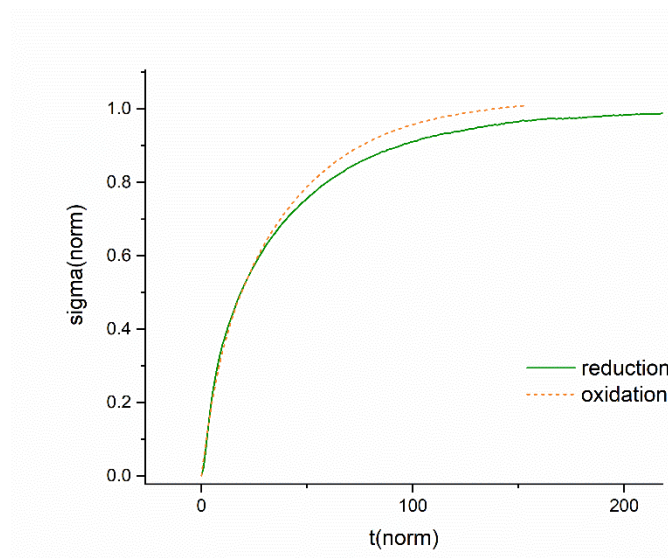
Figure 16 | Relaxation curves for the oxidation and reduction of BCFY262 at 700°C

4 Results and discussion

4.1 Crystal structure

The initial composition $BaCe_{0.5}Fe_{0.5}O_{3-\delta}$ on which this work is based, decomposes into a cerium-rich phase with orthorhombic crystal structure (*Pmcn*) and an iron-rich phase with cubic crystal structure (*Pm-3m*). Figure 17 shows the powder diffraction pattern and the Rietveld refinement of the self-generated composite BCFY442. By adding yttrium to the material, the Ce-rich phase becomes trigonal with the space group *R-3c*. The Fe-rich phase remains cubic, no matter how much Y is added. All measured reflexes could be attributed to the trigonal and cubic phase, respectively, and do not indicate secondary phases. BCFY442 is two-phase and consists of 50 wt-% trigonal phase and 50 wt-% cubic phase. XRD analyses are carried out for all samples discussed in this work and their powder diffraction patterns can be found in the appendix. Table 5 shows the weight percentages of each phase for all samples.
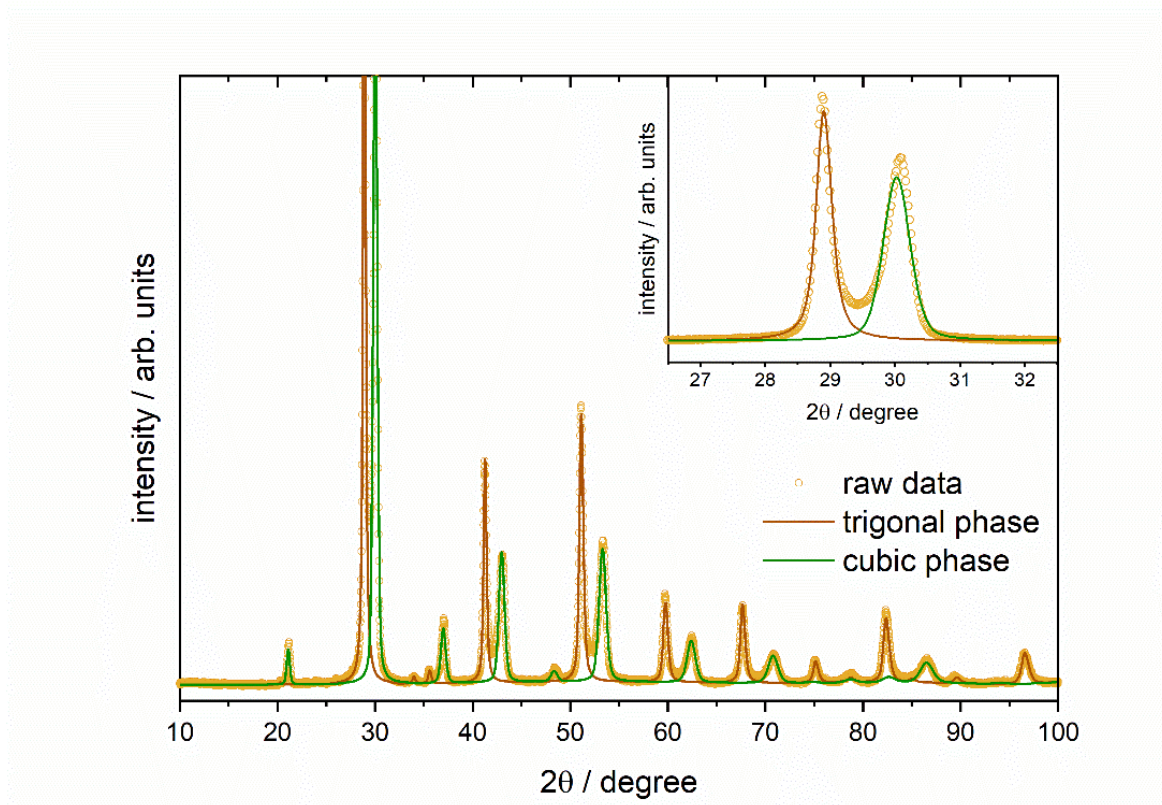
Figure 17 | Powder diffraction pattern (circles) and Rietveld refinement (solid lines) of BCFY442

Table 5 | Phase composition of BCFY262, BCFY442 and BCFY622

	Abbreviation	Trigonal phase (*R-3c*) [wt-%]	Cubic phase (*Pm-3m*) [wt-%]
$BaCe_{0.2}Fe_{0.6}Y_{0.2}O_{3-\delta}$	BCFY262	10	90
$BaCe_{0.4}Fe_{0.4}Y_{0.2}O_{3-\delta}$	BCFY442	50	50
$BaCe_{0.6}Fe_{0.2}Y_{0.2}O_{3-\delta}$	BCFY622	90	10

Figures 18 and 19 display the powder diffraction patterns of $BaCe_{0.8-x}Fe_xY_{0.2}O_{3-\delta}$ ($0.1 \leq x \leq 0.6$) and $BaCe_{0.5}Fe_{0.5}O_{3-\delta}$. With increasing Fe content, the intensity of the reflexes of the cubic phase ($2\theta \cong 30°$, $43°$) increase and those from the trigonal phase ($2\theta \cong 29°$, $41°$) decrease. This is consistent with the expected increase in cubic phase due to increasing Fe content. As shown in Figure 19, a second effect occurs due to the introduction of Y in the material. The cubic reflexes of the Y-free sample appear at larger angles than those of the samples containing Y. In addition, the reflexes of the cubic phase shift towards larger angles with increasing iron content.
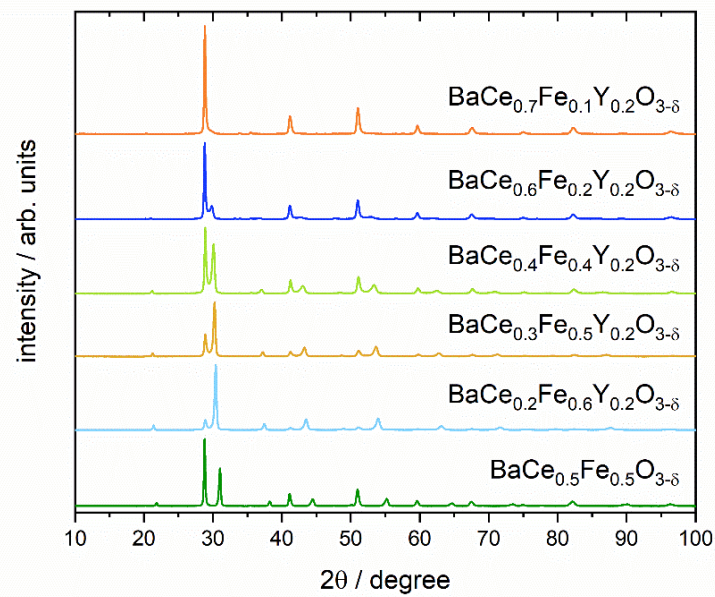
Figure 18 | Powder diffraction patterns of $BaCe_{0.8-x}Fe_xY_{0.2}O_{3-\delta}$ ($0.1 \leq x \leq 0.6$) and $BaCe_{0.5}Fe_{0.5}O_{3-\delta}$
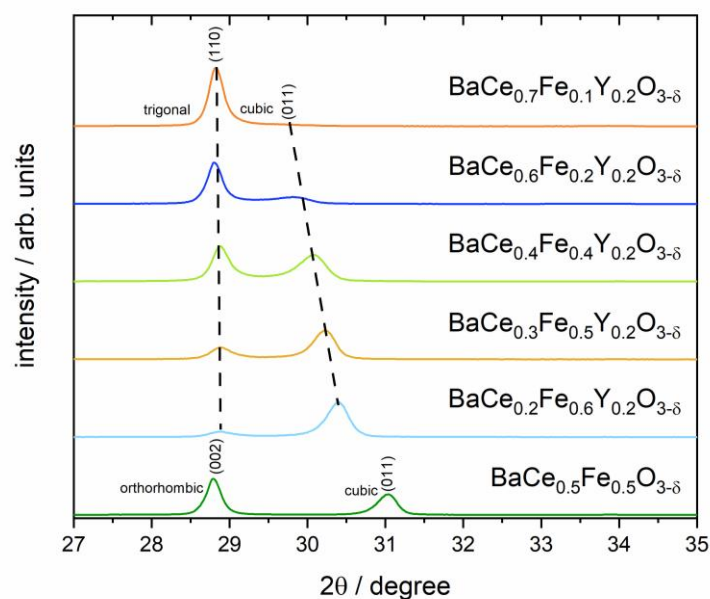
Figure 19 | Main reflexes in detail

Figure 20 displays the (pseudo)-cubic lattice parameters as a function of the Ce content. The pseudo-cubic lattice parameter for the trigonal phase is calculated using Equation 15. Two things can be noticed. Firstly, the addition of Y mainly affects the lattice parameter of the Fe-rich cubic phase. Secondly, the lattice parameter and thus the volume of the unit cell of the cubic phase increases with increasing Ce content. The first effect can be explained by the ionic radii of the ions on the B-site. Cerium and yttrium (Ce^{4+} (VI) (0.87 Å); Y^{3+} (VI) (0.900 Å) [20]) have similar ionic radii, which is why the lattice parameter of the trigonal (Ce-rich) phase is only weakly affected by the addition of Y. However, iron (Fe^{4+} (0.725 Å); Fe^{3+} (0.785 Å) [20]) has a much smaller ionic radius. Thus, the lattice parameter of the cubic (Fe-rich) phase is increased by adding Y. The second effect, the increase in the lattice parameter of the cubic phase with increasing Ce content, can be explained by the preferential incorporation of Y into the Fe-rich phase, which will be shown in detail in section 4.4. By increasing the Ce content, the amount of Y in the Fe-rich phase increases, resulting in an increased lattice parameter of the cubic phase.
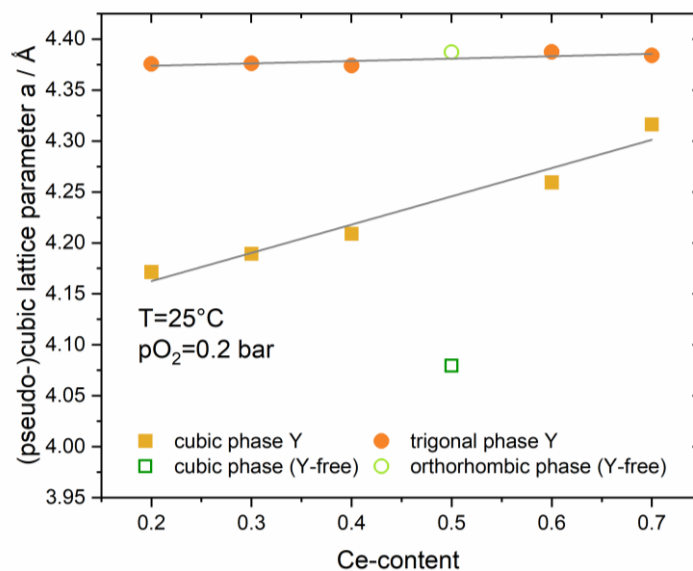
Figure 20 | (Pseudo)-cubic lattice parameters of $BaCe_{0.8-x}Fe_xY_{0.2}O_{3-\delta}$ (0.1≤x≤0.6) and $BaCe_{0.5}Fe_{0.5}O_{3-\delta}$

Equation 15 | Formula for the pseudo-cubic lattice parameter

4.2   Electrical conductivity

Electrical conductivity measurements in dry and humid atmosphere were carried out for the self-generated composites BCFY442, BCFY622 and BCFY262. In Figure 21 the electrical conductivity σ and ln σT (Arrhenius plots) of BCFY442 are given as function of temperature. The activation energies of σ were determined from the slope of the Arrhenius plots and can be found in Table 6, where the activation energies of all samples are summarised. BCFY442 shows similar activation energies under the two conditions. In dry atmosphere, the activation energy is 32.8 ± 1.1 kJ mol^{-1} and in humid atmosphere it is 34.0 ± 1.7 kJ mol^{-1}. As the electronic conductivity (small polaron hopping mechanism) exhibits a thermally activated nature, σ increases with increasing temperature, which is consistent with our observations. As expected according to Equation 5, the σ values at an oxygen partial pressure of 0.15 bar are higher than those at 0.10 bar. A higher pO$_2$ favours the incorporation of oxygen and shifts the equilibrium to the right side of the equation. Thereby the number of p-type charge carriers (Fe^{4+}/h$^{·}$) increases, resulting in an increased electronic conductivity.
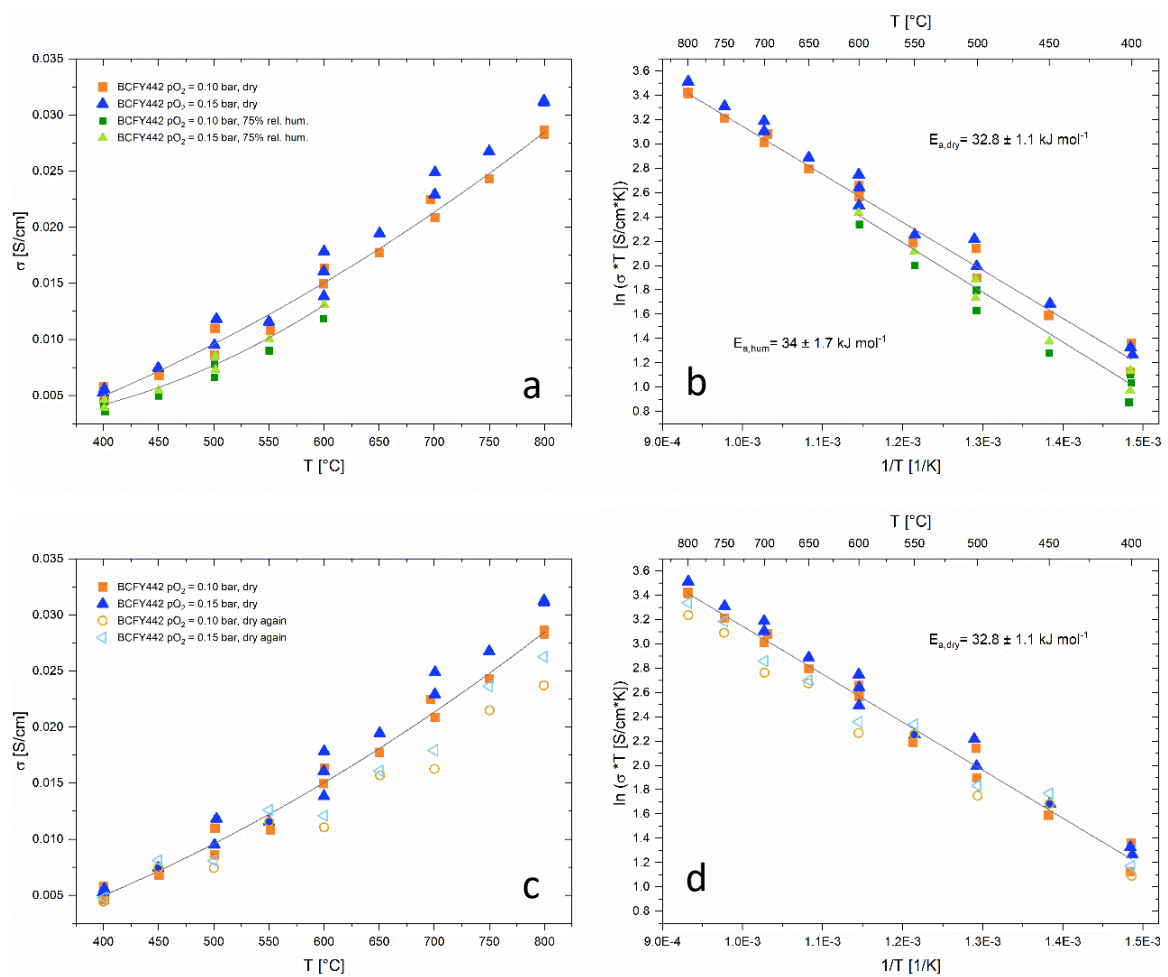
Figure 21 | (a) and (c) Electrical conductivity; (b) and (d) Arrhenius plots of BCFY442 in dry and humid atmosphere

In humid atmosphere, the electrical conductivity is reduced, as shown in Figure 21a (green symbols). This is consistent with Equation 6, describing a decrease in the number of charge carriers ($Fe^{4+}/h^{\cdot}$) due to proton incorporation. In fact, however, this may not be the only reason for the decrease in electrical conductivity, which is discussed in more detail in section 4.4. Figure 21c displays the electrical conductivity before and after the sample was exposed to a humid atmosphere. The conductivity values after humidification do not return to the original range but remain at a level similar to that in humid atmosphere.

Figure 22a displays the electrical conductivity of BCFY622 as function of temperature in dry and humid atmosphere. It shows the same trends in T- and pO_2-dependence of σ as the sample BCFY442. However, the electrical conductivity increases slightly more with temperature and the dependence on pO_2 is not as strong. In general, the conductivity values of BCFY622 are about one order of magnitude lower than those of BCFY442. Since sample BCFY622 consists of only 10 wt-% cubic phase (the main electronic conducting phase), this is in good agreement with the expectations. In humid atmosphere, the electrical conductivity is also reduced, but much less than at BCFY442.
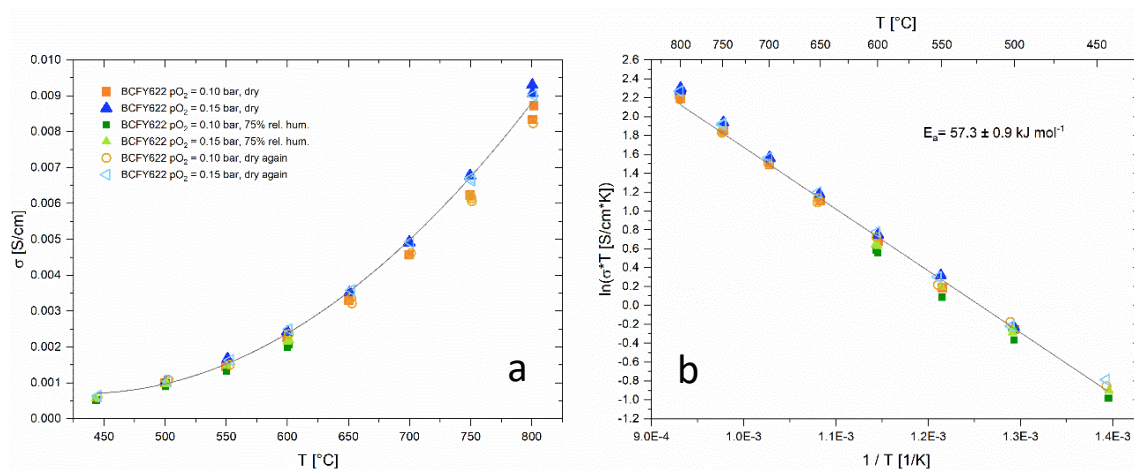
Figure 22 | (a) Electrical conductivity and (b) Arrhenius plot of BCFY622 in dry and humid atmosphere

In Figure 23a the electrical conductivity of BCFY262 is given as function of temperature. It also shows the same trends in T- and pO_2-dependence of σ as the other samples but the increase in electrical conductivity with temperature is smaller compared to the other composites. Instead, the dependence on pO_2 is much stronger. The curves in both plots are fitted with the values for 0.10 bar oxygen partial pressure. Generally, the conductivities of BCFY262 are one order of magnitude higher than those of BCFY442. This agrees well with the fact that BCFY262 consists of 90 wt-% cubic phase. In humid atmosphere, the electronic conductivity of BCFY262 seems to be particularly strongly reduced in comparison to BCFY622 and BCFY442. However, the measurements on this sample have not yet been completed and further tests are still necessary to determine the activation energy of σ.
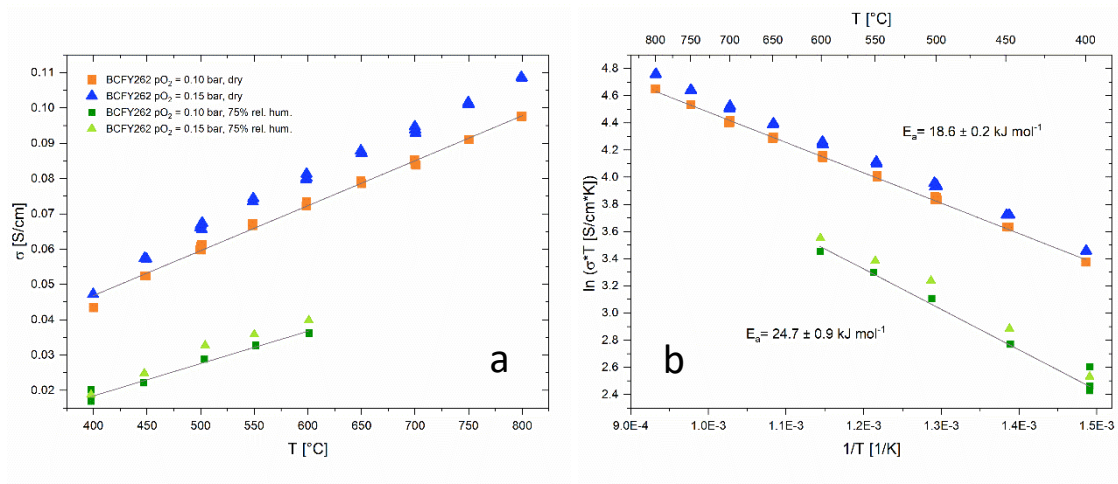
Figure 23 | (a) Electrical conductivity and (b) Arrhenius plot of BCFY262 in dry and humid atmosphere
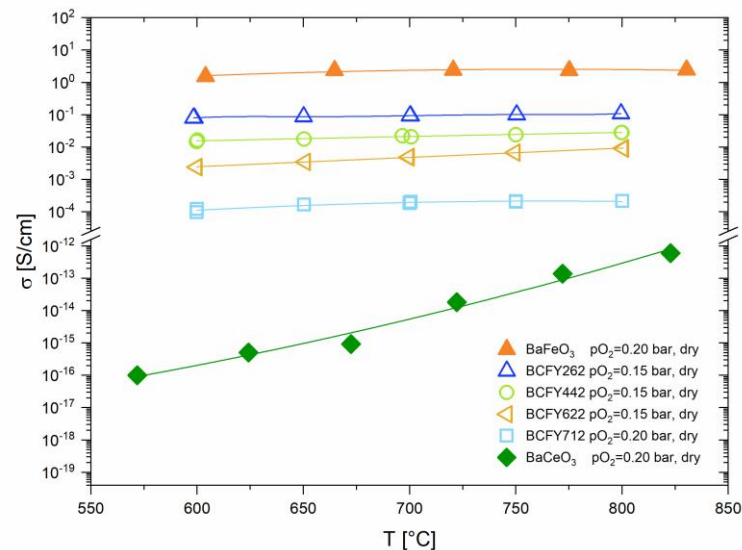
Figure 24 | Electrical conductivity of BaCe$_{0.8-x}$Fe$_x$Y$_{0.2}$O$_{3-\delta}$ (0.1≤x≤0.6) in comparison with BaFeO$_3$ [37] and BaCeO$_3$ [38] in dry atmosphere

Figure 24 shows σ as function of temperature for different compositions and their comparison to σ of BaCeO$_3$ and BaFeO$_3$. The electrical conductivity increases as expected with an increasing amount of Fe in the material, as the Fe-rich phase is the main electronic conducting phase. The comparison of the three samples analysed shows a correlation between the Fe content and the reduction of the electronic conductivity in humid atmosphere. With increasing Fe content, the reduction in electrical conductivity becomes more pronounced. The extent of the T- and pO$_2$-dependence is also related to the Fe content in the composites. With increasing Fe content, the difference of the conductivity values at different oxygen partial pressures becomes larger. In contrast, the increase in σ with increasing temperature is less significant for composites with higher Fe content.

Table 6 | Activation energies of σ in dry atmosphere of BCFY262, BCFY442 and BCFY622

	Activation energy [kJ mol^{-1}]
BaCe$_{0.2}$Fe$_{0.6}$Y$_{0.2}$O$_{3-\delta}$	18.6 ± 0.2
BaCe$_{0.4}$Fe$_{0.4}$Y$_{0.2}$O$_{3-\delta}$	32.8 ± 1.1
BaCe$_{0.6}$Fe$_{0.2}$Y$_{0.2}$O$_{3-\delta}$	57.3 ± 0.9

Table 6 shows the activation energies of σ of all samples in dry atmosphere. The activation energy of BCFY442 is by factor ~ 2 larger than that of BCFY262. The one of BCFY622 is by factor ~2 larger than the activation energy of BCFY442. Figure 25 shows log(σ*T) as function of temperature. The values of BaCe$_{0.8}$Y$_{0.2}$O$_3$ and BaCeO$_3$ can be found on the axes on the right-hand side. Our data fits well with BaCe$_{0.8}$Y$_{0.2}$O$_3$ and BaFeO$_3$ in terms of slope. BCFY712 shows a similar change in slope as BaFeO$_3$ at about 650°C.
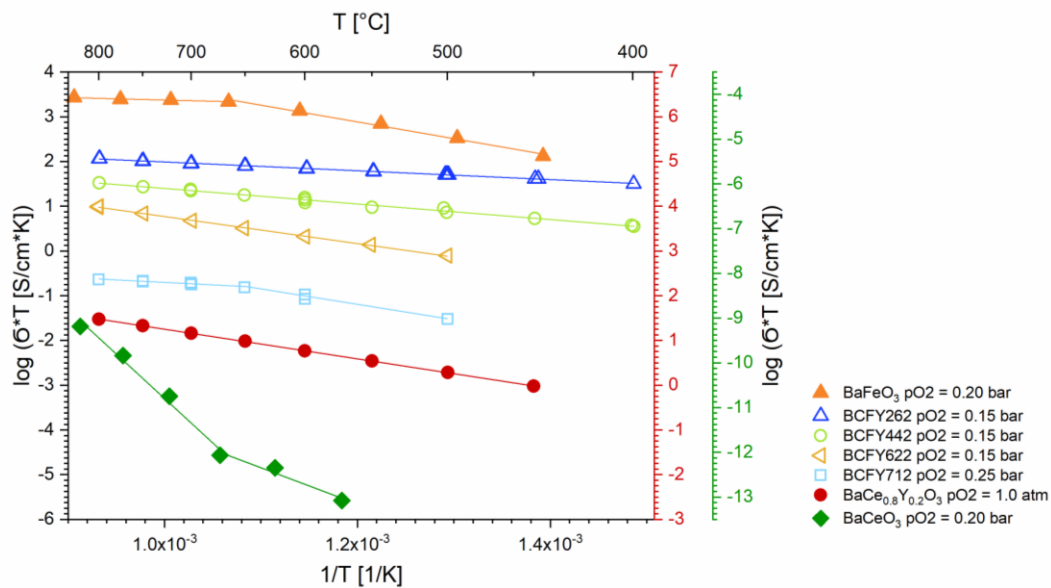
Figure 25 | Plot of log(σ*T) vs. 1/T of BaCe$_{0.8-x}$Fe$_x$Y$_{0.2}$O$_{3-\delta}$ (0.1≤x≤0.6) in comparison with BaFeO$_3$ [37], BaCeO$_3$ [38] and BaCe$_{0.8}$Y$_{0.2}$O$_3$ [39] in dry atmosphere

4.3   Oxygen exchange kinetics

The conductivity relaxation technique described in more detail in section 2.4.3. and 3.3. is used to determine the temperature dependence of the chemical diffusion coefficient of oxygen. Assuming fast oxygen surface exchange reaction or a sufficiently large sample thickness, the oxygen exchange kinetics is diffusion-controlled (which is mostly the case in this work) [40]. The composites exhibit three different charge carriers, which are oxygen vacancies, electron holes and protonic defects. Since the concentration of protonic defects is very small at higher temperatures (T≥500°C), their contribution to D_{chem} can be neglected and it is assumed that D_{chem} represents the diffusion of oxygen. Nevertheless, the diffusion coefficients are effective values, as the samples consist of two phases and it is not possible to identify the contribution of each phase with this technique.

For BCFY442, the oxygen exchange kinetics is diffusion-controlled and results could be obtained for all temperatures and oxygen partial pressures. Figure 26 shows the normalised conductivity relaxation curves of BCFY442 at different temperatures in a range of 400 ≤ T/°C ≤ 800. The elapsing time to reach complete relaxation becomes shorter with increasing temperatures, which means that D_{chem} increases with increasing temperature. This is consistent with the Arrhenius plots of the chemical diffusion coefficient of oxygen shown in Figure 27. D_{chem} is given as function of temperature upon oxidation and reduction and the results for both processes are in good agreement. The activation energies of D_{chem} are calculated from the slope of the Arrhenius plots and are given in Table 7. As shown in Figure 27a, it seems that the values for D_{chem} in humid atmosphere (green symbols) are increasing. Once they have reached a certain maximum, they remain at this new level and show an activation energy similar to that in dry atmosphere. Figure 27b shows the values for D_{chem} in dry atmosphere before and after humidification. The chemical diffusion coefficient seems to be increased to a higher level by humidification and remains at this level after drying. These observations are discussed in detail in section 4.4.
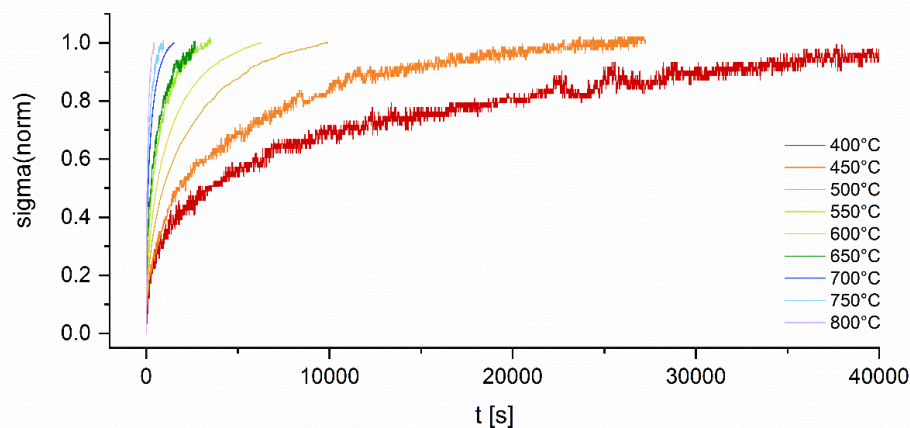
Figure 26 | Relaxation curves of BCFY442 in a temperature range of 400 ≤ T/°C ≤ 800°
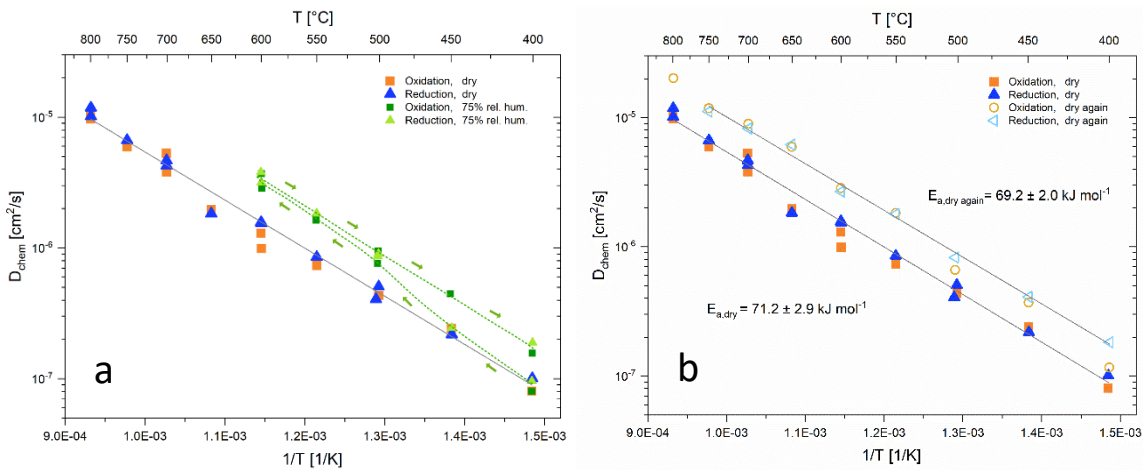
Figure 27 | Arrhenius plots of the chemical diffusion coefficient of oxygen of BCFY442 in dry and humid atmosphere

For BCFY622, the oxygen exchange kinetics is also rate-limited by diffusion. Measurements are carried out in dry and humid atmosphere in the full temperature range. However, the data of measurements below a temperature of 550°C and those in humid atmosphere could not be evaluated. The measured change in resistance in humid atmosphere at 500°C is shown in Figure 28a. A curve like this can not be evaluated, as no defined end of relaxation can be identified. Therefore, results are only available for a temperature range of $550 \leq T/°C \leq 800$ in dry atmosphere. Figure 28b shows the chemical diffusion coefficient of oxygen of BCFY622 as function of temperature. The activation energy calculated from the slope of the Arrhenius plot can be found in Table 7. It is higher than that of BCFY442. The diffusion coefficients in dry atmosphere after humidification seems to be slightly decreased. In order to find an explanation for this, STEM and EDX analysis on the aged sample are planned in the future.
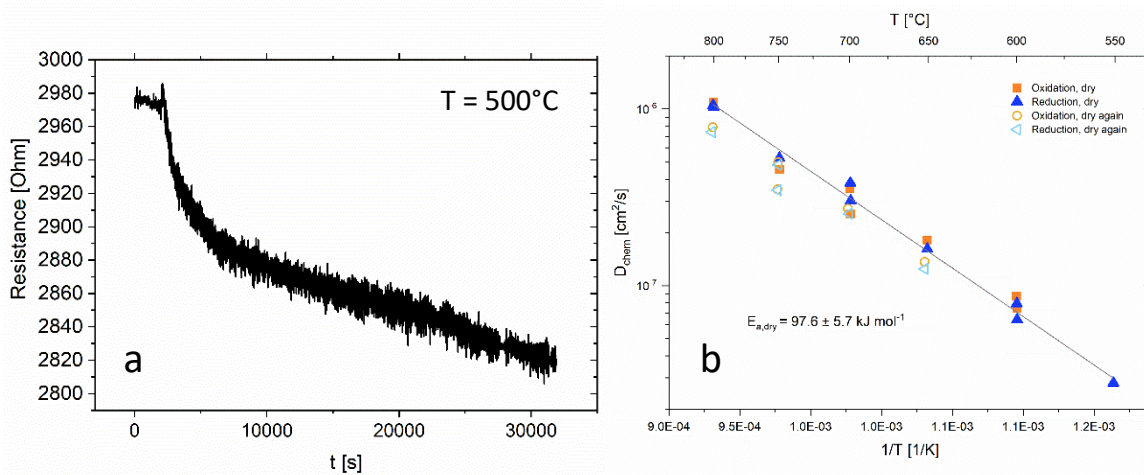
Figure 28 | (a) Relaxation in resistance of BCFY622 at 500°C in humid atmosphere and (b) Arrhenius plot of the chemical diffusion coefficient of oxygen of BCFY622 in dry atmosphere
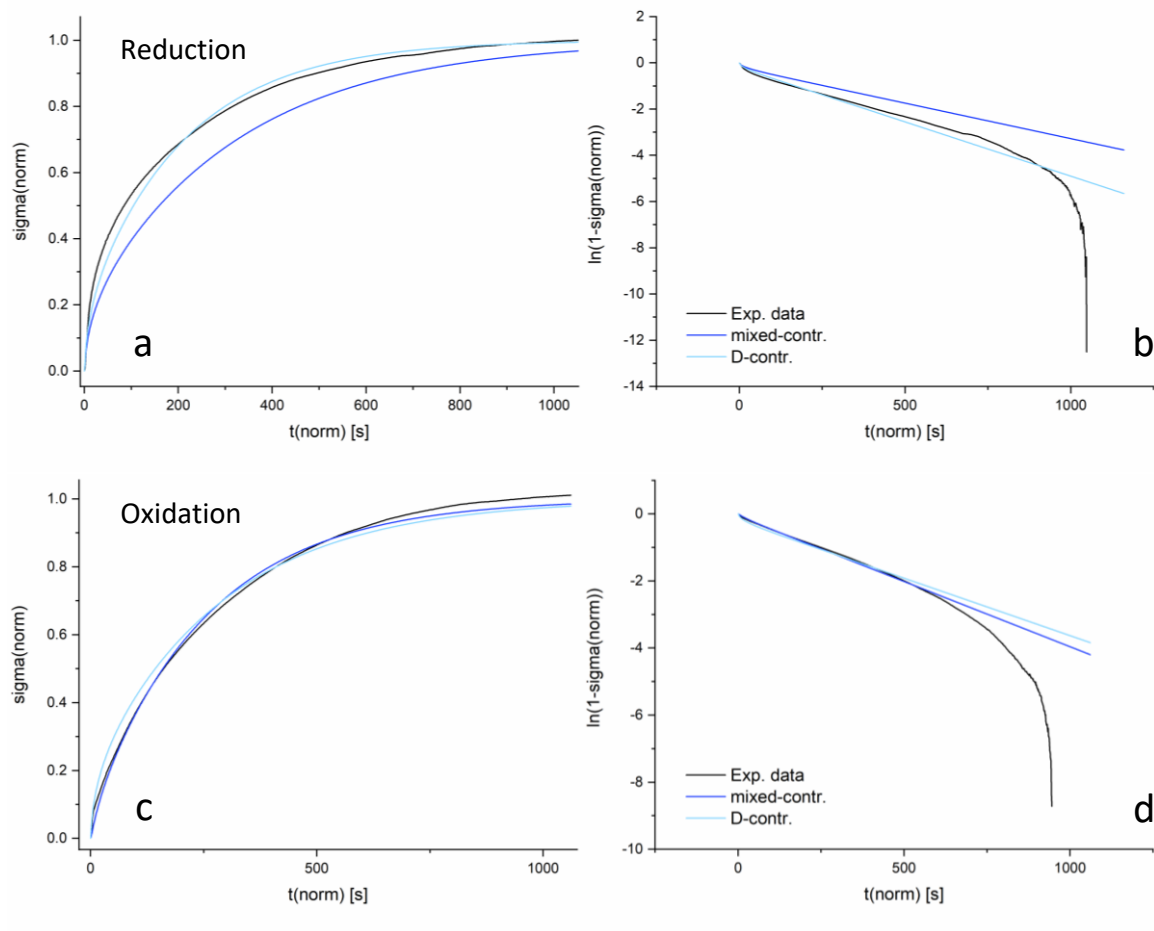
Figure 29 | σ norm and ln(1- σ norm) vs. tnorm of BCFY262 at T=500°C in dry atmosphere for the (a) and (b) reduction and (c) and (d) oxidation with fits to equations for diffusion-controlled and mixed-controlled kinetics

In the temperature range of 600 ≤ T/°C ≤ 800 the oxygen exchange kinetics of BCFY262 is diffusion-controlled. Figure 29a and c show the normalised conductivity relaxation curves of BCFY262 for the reduction and the oxidation process at 500°C. The corresponding fits for diffusion-limited kinetics are displayed in light blue and those for mixed controlled kinetics in dark blue. Figure 29a shows a good agreement with the fit to the model for diffusion-controlled kinetics for the reduction, as it does for all measurements at higher temperatures. However, Figure 29c shows a better match with the fit to the model for mixed-controlled kinetics for the oxidation. This is the case for all oxidation processes at T ≤ 550°C. For the oxidation, the values of D_{chem} in this temperature range are obtained from mixed-controlled fits. The chemical diffusion coefficient of oxygen of BCFY262 is shown in Figure 30 as function of temperature. The activation energy in dry atmosphere is obtained from the slope of the Arrhenius plot and is lower than that of BCFY442. In humid atmosphere, the relaxation curves of BCFY262 could not be described by the fitting functions used. This could be a result of a similar effect occurring at BCFY442, which is described in more detail in section 4.4. However, whether this is actually the case can only be determined after post-test STEM and EDX analysis.
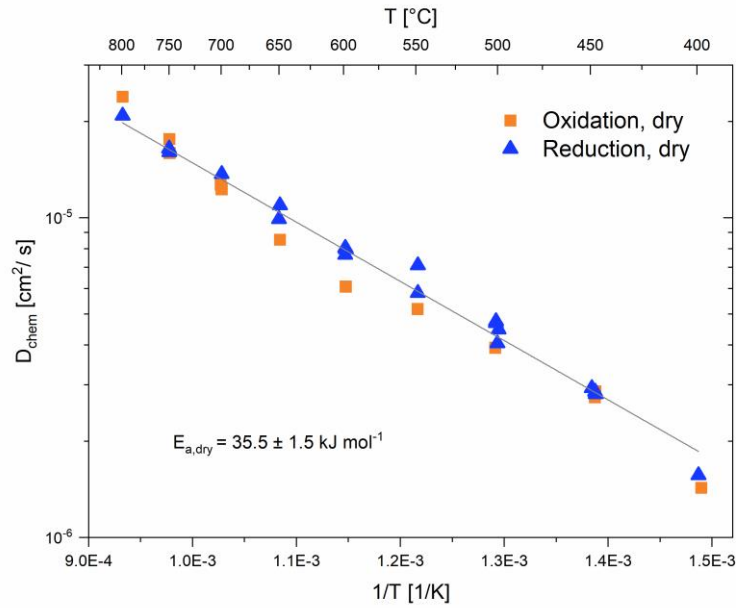
Figure 30 | Arrhenius plot of the chemical diffusion coefficient of oxygen of BCFY262 in dry and humid atmosphere

Figure 31 displays D_{chem} of different composites from the BCFY series as function of temperature in comparison with those of mixed oxygen ionic-electronic conducting SOFC cathode materials. In the BCFY series, the chemical diffusion coefficient increases with increasing Fe content. This is expected, as the main oxygen ion-conducting phase is the cubic phase, which is rich in Fe. The activation energy for D_{chem} increases with decreasing Fe content, as shown in Table 7.
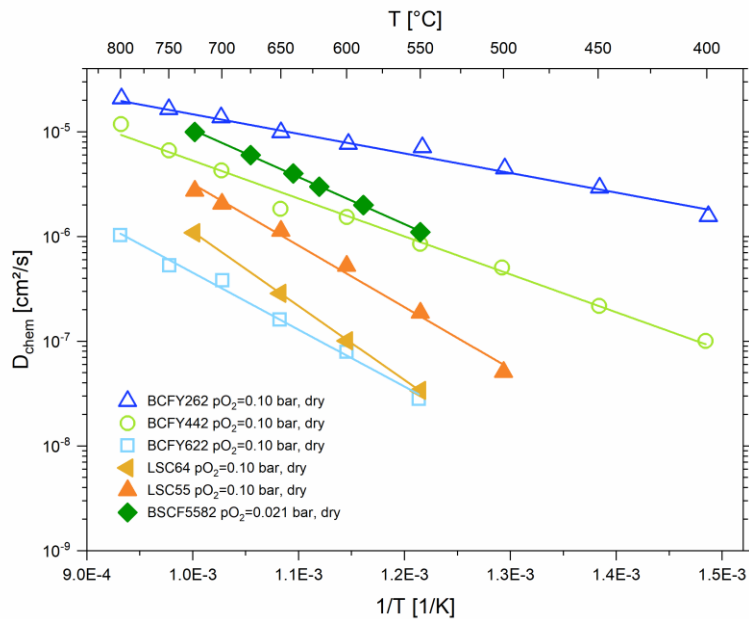
Figure 31 | Arrhenius plot of the chemical diffusion coefficient of oxygen of $BaCe_{0.8-x}Fe_xY_{0.2}O_{3-\delta}$ (0.2≤x≤0.6) compared with $La_{0.6}Sr_{0.4}CoO_{3-\delta}$ [41], $La_{0.5}Sr_{0.5}CoO_{3-\delta}$ [41] and $Ba_{0.5}Sr_{0.5}Co_{0.8}Fe_{0.2}O_{3-\delta}$ [42] in dry atmosphere

Table 7 | Activation energies of D_{chem} in dry atmosphere of BCFY262, BCFY442 and BCFY622

	Activation energy [kJ mol^{-1}]
$BaCe_{0.2}Fe_{0.6}Y_{0.2}O_{3-\delta}$	35.5 ± 1.5
$BaCe_{0.4}Fe_{0.4}Y_{0.2}O_{3-\delta}$	71.2 ± 2.9
$BaCe_{0.6}Fe_{0.2}Y_{0.2}O_{3-\delta}$	97.6 ± 5.7

4.4 Transmission electron microscopy

4.4.1 Basic characterisation

Scanning transmission electron microscopy (STEM) and energy-dispersive X-ray spectrometry (EDX) analyses were conducted by Judith Lammer at Centre for Electron Microscopy Graz. Only a few images are discussed in this chapter as examples, the rest can be found in the appendix. Figure 32 shows the high-angle annular dark-field (HAADF) image of BCFY262 in two different magnifications. The sample is placed into a sample holder (SiN) and fixed with platinum (light region at the lower end of the sample). With this method, heavy elements are displayed as brighter areas in the image and light elements as darker areas. Particularly dark areas are usually breakouts or holes in the sample. The brighter areas in Figure 32 are grains rich in Ce and the dark areas are Fe-rich grains. As expected, a large part of the cross-section analysed is composed of dark areas. This is consistent with the ratio of Fe-rich to Ce-rich phase (90:10). Apart from a few small holes or breakouts, the sample is dense and there are no anomalies in this part of the sample.
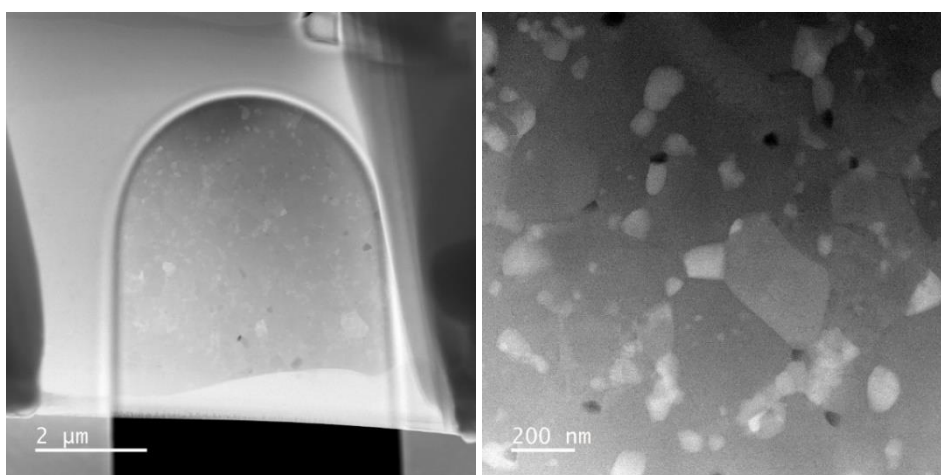
Figure 32 | STEM-HAADF images of BCFY262

To determine the stoichiometric composition and the distribution of the elements, EDX point spectra and STEM-EDX elemental maps of Ba, Ce, Fe and Y were acquired. The element distribution of the BCFY series is discussed using BCFY442 as an example. The described properties are characteristic for all samples. Figure 33 displays the element distribution of BCFY442 after the EC/CR measurement run. As shown in Figure 33b, Ba is homogeneously distributed in both phases. The comparison of Figure 33a, d, e and f shows the enrichment of Fe in one phase (dark areas in the HAADF image) and Ce in the other phase (light areas in the HAADF image). This is exactly what we expected, as the composite consists of an Fe-rich and a Ce-rich phase. Y is preferentially found in the Fe-rich phase, as shown in Figure 33c.
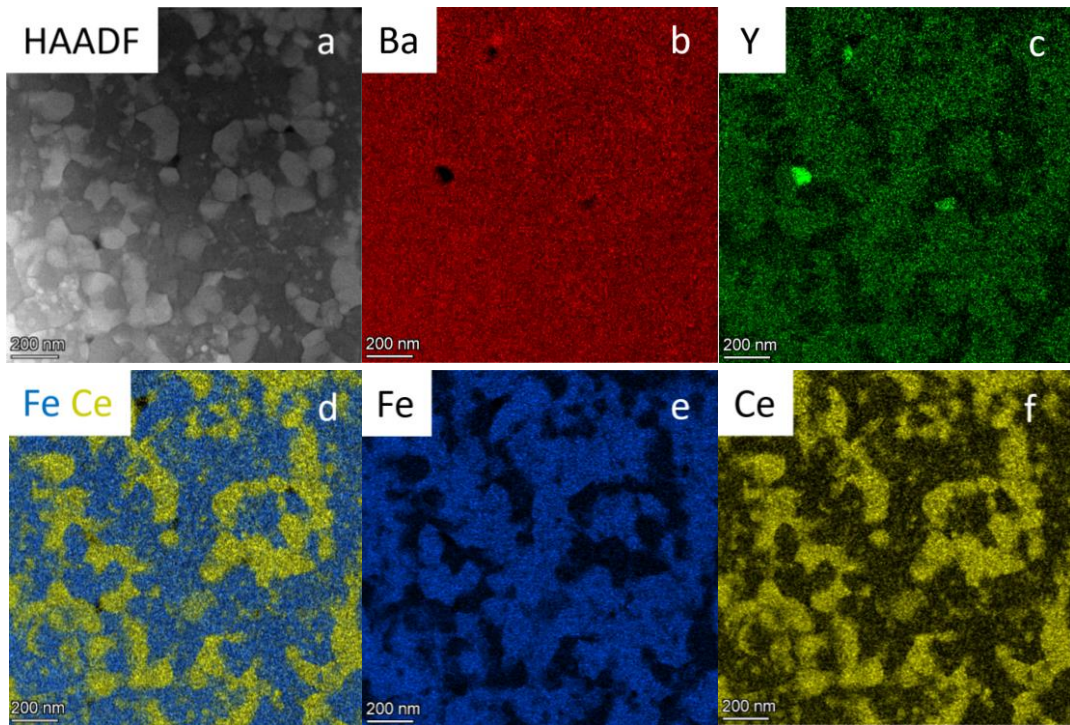
Figure 33 | STEM-EDX elemental maps of Ba, Fe, Ce and Y in the composite BCFY442 (post-test)

4.4.2   Post-test analysis

STEM and EDX analysis were carried out for BCFY442 on a fresh sample and on a sample that had undergone a full EC/CR measurement run. The exact parameters during the EC/CR measurements are as follows. The sample stays 52 days in dry atmosphere in a temperature range of 400 ≤ T/°C ≤ 800. Then it is equilibrated in 75% relative humidity for 10 days before the beginning of the measurements in humidified atmosphere in a temperature range of 400 ≤ T/°C ≤ 600. In total, the sample remains in the humidified atmosphere for 46 days. Afterwards, the sample is dried for 10 days and then the measurements in dry atmosphere start again. The sample remains in dry atmosphere for a total of 44 days in a temperature range of 400 ≤ T ≤ 800°C and is then removed from the test unit.
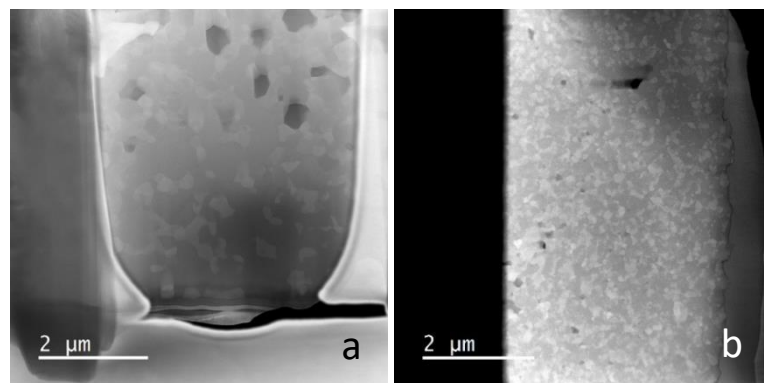
Figure 34 | STEM-HAADF images of BCFY442 (a) fresh and (b) post-test

Figure 34a and b display the cross-section analysed of the samples before and after EC/CR measurements in the same magnification. After exposure to a humid atmosphere at high temperatures, the grain size is smaller and the microstructure of the composite is finer than before. With the images obtained, a grain size analysis was carried out. The results are shown in Figure 35. The central small circle shows the average minimum diameter of the grains and the large half-filled circle shows the average maximum diameter. Figure 36 displays the selected grains for the grain size analysis. The Fe-rich grains are marked in red and the Ce-rich grains in orange. Additionally, there are small grains rich in Ce in the post-test sample marked in yellow. The origin of these extra grains will be discussed later. As shown in Figure 36, the particles are not perfectly circular and show significant variations in size. Therefore, the difference between the minimum and maximum diameters and the standard deviation are relatively large.

Fe-rich   **Ce-rich**

FRESH $250 \pm 110 \leq d/nm \leq 452 \pm 170$ $154 \pm 54 \leq d/nm \leq 276 \pm 94$

POST-TEST $104 \pm 46 \leq d/nm \leq 182 \pm 72$ $84 \pm 34 \leq d/nm \leq 140 \pm 52$ $22 \pm 6 \leq d/nm \leq 36 \pm 12$
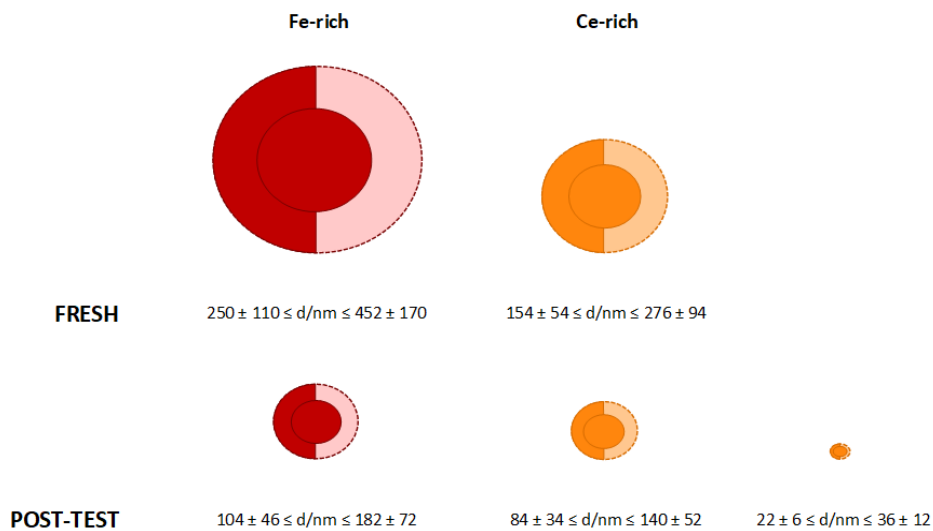
Figure 35 | Average grain size of Fe-rich particles (red) and Ce-rich particles (orange) of fresh and post-test BCFY442 samples
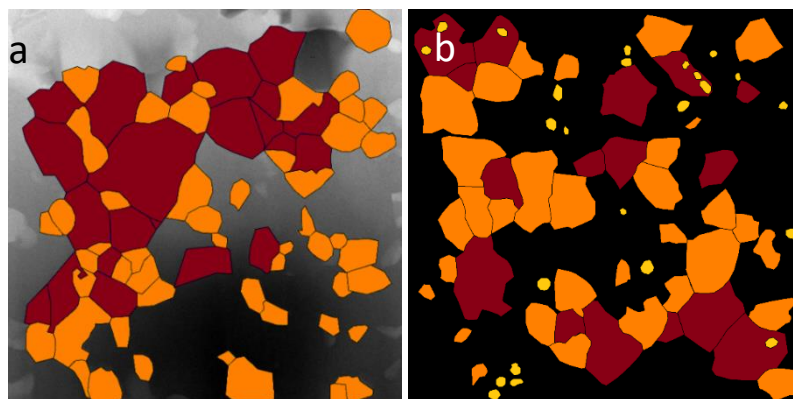
Figure 36 | Selected grains for the grain size analysis of BCFY442 (a) fresh and (b) post-test, Fe-rich grains in red and Ce-rich grains in orange and yellow (precipitations)
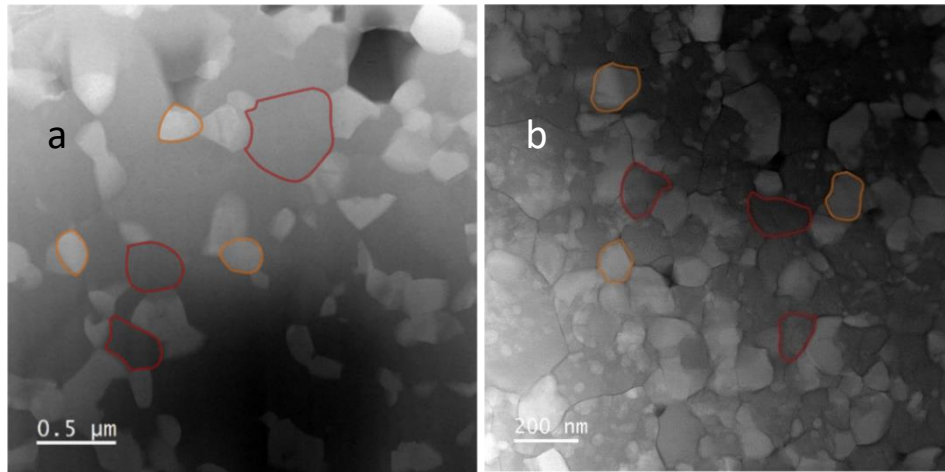
Figure 37 | STEM-HAADF images of BCFY442 (a) fresh and (b) post-test, the Fe-rich phase is highlighted in red and the Ce-rich phase highlighted in orange

At higher magnification, as shown in Figure 37a and b, two additional effects occurring during the EC/CR measurements can be seen. In the dark matrix of the Fe-rich phase, small brighter grains rich in Ce are formed. Additionally, dark regions appear at the grain boundaries. The analysis of the chemical composition by EDX shows a difference between the two samples. In Table 8, the proportions of the elements in the two phases calculated from EDX results are shown. The Fe-rich phase of the composite after the measurement run has a lower Ce content than before. Furthermore, the Ce-rich phase shows an increased variation in the Ce content, and the Y content is slightly higher in both phases. This leads to the assumption that the Fe-rich phase (highlighted in red) is not stable under humid conditions in a higher temperature range. It precipitates parts of the Ce resulting in a decreased Ce amount in the surrounding Fe-rich phase. The precipitated Ce forms the small Ce-rich grains to be seen in Figure 36b (marked in yellow) and Figure 37b. However, the Ce-rich phase seems to be stable under humid conditions and high temperatures, as no phase separation could be identified there.

Table 8 | Chemical composition of BCFY442 composites before and after EC/CR measurements

		Fe concentration [%]	Ce concentration [%]	Y concentration [%]
fresh	Fe-rich phase	57 ± 2	23 ± 1	20 ± 1
	Ce-rich phase	9 ± 2	86 ± 3	5 ± 1
post-test	Fe-rich phase	56 ± 2	17 ± 4	25 ± 1
	Ce-rich phase	9 ± 4	79 ± 19	8 ± 2

The second observed change, i.e. the dark regions at the grain boundaries shown in Figure 37b, is presumably related to the phase separation. Figure 38 displays EDX line scans across a grain boundary.
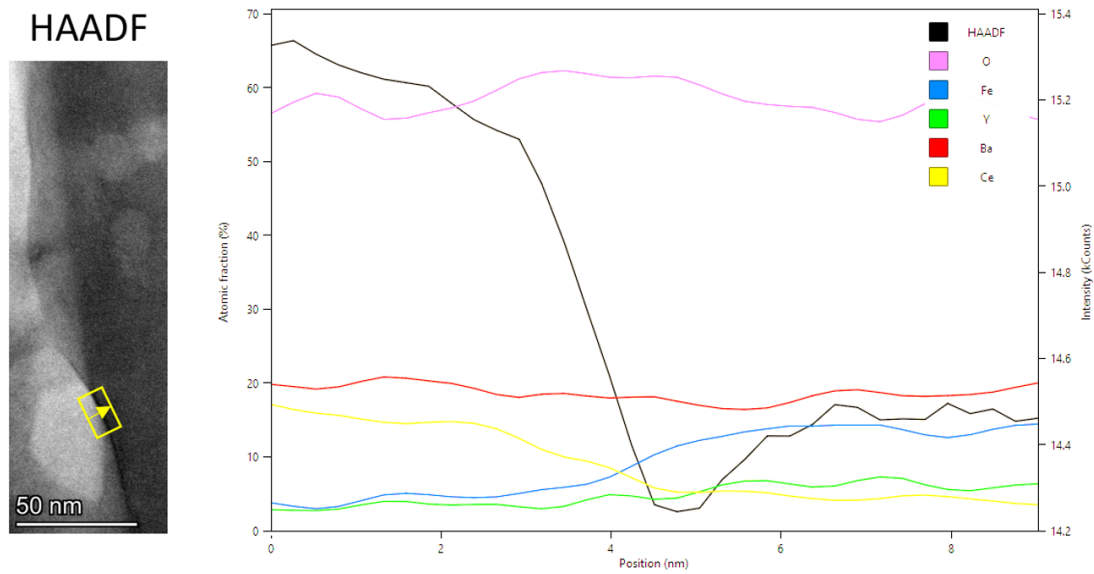
Figure 38 | EDX profile across a grain boundary in BCFY442 (post-test)

According to the EDX profile, the grain boundary considered divides a Ce-rich particle from an Fe-rich particle. The amount of Fe increases in the region of the reduced HAADF signal and the amount of Ce decreases. Regarding Y, a slight increase can be observed in this region. There is no enrichment or depletion of any element at the grain boundary. Thus, the reduced HAADF signal indicates a crack at the grain boundary. The occurring phase separation in the Fe-rich phase may lead to a change in volume, which may causes mechanical stress and thus induce cracks at the grain boundaries. Figure 39 shows further HAADF images of a crack at the grain boundary in different magnifications.
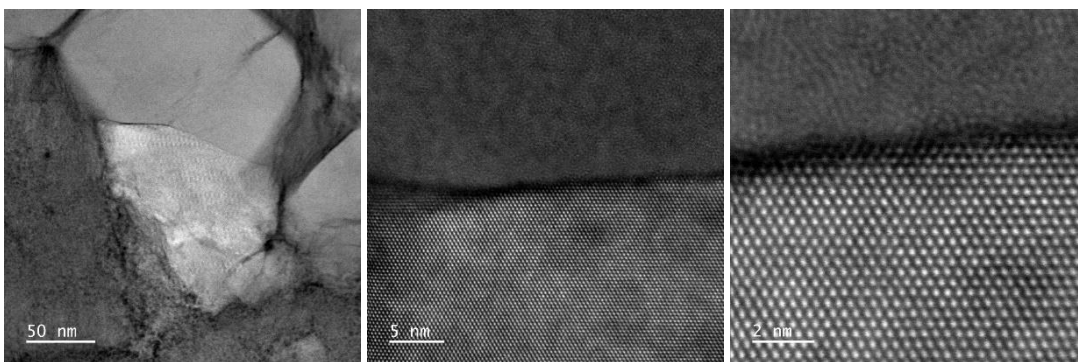
Figure 39 |STEM- HAADF images of a crack at a grain boundary in BCFY442 (post-test)

These observations are consistent with the results given in section 4.2 and 4.3. As shown in Figure 40, the sample exhibits reduced electrical conductivity and apparently increased oxygen diffusion after humidification. These changes in properties are permanent, as the values for σ and D_{chem} do not return to the initial level.
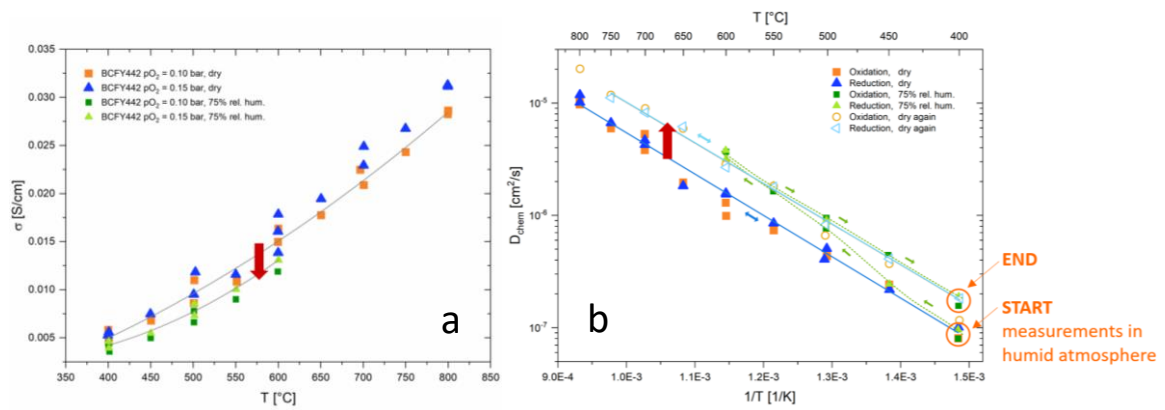
Figure 40 | (a) Electrical conductivity and (b) chemical diffusion coefficient of oxygen as function of temperature of BCFY442 in dry and humid atmosphere

In Figure 41, the proposed mechanisms for the changes occurring during humidification are shown in detail. Through phase separation in the Fe-rich phase, cracks appear at the grain boundaries. These cracks interrupt electrically conductive paths in the material (dashed line in green). As a result, only a part of the previously available conducting pathways is available for the transport of electrons, leading to reduced electrical conductivity. The increase in D_{chem} in humid atmosphere may not be real in the case of BCFY442, because the change is permanent. Before humidification, the oxygen passed through the bulk. The apparent increase in D_{chem} may be related to phase separation and the associated cracks in humid atmosphere, not to proton incorporation. The measurements in dry atmosphere after humidification remain at the same level as in humid atmosphere. It is assumed that the oxygen is no longer transported solely through the bulk (solid state transport) but partly through the cracks along the grain boundaries (gas phase transport; solid line in blue), as shown in Figure 41.
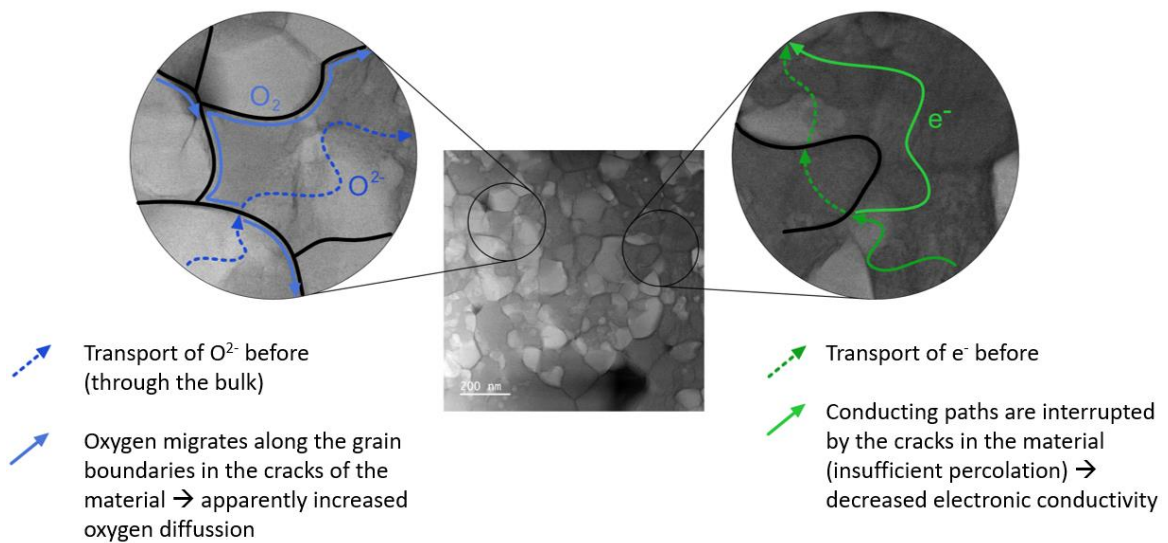
Figure 41 | Transport paths of O^{2-} and e^- before and after humidification

5   Conclusion

Three different composites, $BaCe_{0.4}Fe_{0.4}Y_{0.2}O_{3-\delta}$ (BCFY442), $BaCe_{0.6}Fe_{0.2}Y_{0.2}O_{3-\delta}$ (BCFY622) and $BaCe_{0.2}Fe_{0.6}Y_{0.2}O_{3-\delta}$ (BCFY262), were synthesised and investigated in terms of their chemical composition and mass- and charge transport properties.

The self-generated composites were prepared by one-pot synthesis using the EDTA-citric acid method. XRD, EDX and STEM analyses were employed to check the stoichiometric phase composition and the structure of the materials. The addition of Y transforms the Ce-rich phase with originally orthorhombic crystal structure, into a Ce-rich phase with trigonal crystal structure. All samples were investigated in terms of their electrical conductivity by four-point dc van der Pauw method in dry and humid atmosphere in a temperature range of $400 \leq T/°C \leq 800$ and $0.10 \leq pO_2/bar \leq 0.15$. In dry atmosphere, the electrical conductivities of the composites are in the range of $1 \cdot 10^{-3} \leq \sigma/S\ cm^{-1} \leq 1 \cdot 10^{-1}$. The electrical conductivity increases with increasing Fe-content since the Fe-rich phase is the main electronic conducting phase. In humid atmosphere, the electrical conductivity is reduced. The reason for this effect may not be the decrease in the number of charge carriers due to proton incorporation but the cracks at the grain boundaries. Furthermore, the oxygen exchange kinetics was investigated for all samples in the temperature range of $400 \leq T/°C \leq 800$ in oxidising and reducing direction in dry and humid atmosphere. In the case of BCFY622, problems were encountered in humid atmosphere and at low temperatures. The reason for this could be that this sample may not show the required predominantly electronic conductivity in this environment. BCFY442 showed an apparently increased chemical diffusion coefficient of oxygen in humid atmosphere. However, this may also be a result of the cracks occurring during humidification, as the oxygen now migrates through the cracks along the grain boundaries and no longer through the bulk. The chemical diffusion coefficients of oxygen of the composites in dry atmosphere are in the range of $2 \cdot 10^{-8} \leq D_{chem}/cm^2\ s^{-1} \leq 2 \cdot 10^{-5}$. After a full measurement run, post-test EDX and STEM analyses were carried out on BCFY442. These results showed grain refinement, precipitation of Ce from the Fe-rich phase, and cracks at the grain boundaries. This leads to the assumption that certain composites may not be stable under humid conditions at high temperatures. However, this assumption must subsequently be validated by analysing the other samples. If the phase decomposition in humid atmosphere proves to be true, an application of this property could be considered. For example, this could be utilised by in-situ decomposition of an Fe-rich pure phase into a self-generated triple-conducting composite in humid atmosphere.

Subsequently, further tests concerning the stability and proton uptake of the available samples should be carried out. In order to further improve the materials, the substitution with other ions at the A- or B-site could be considered (e.g. Yb, Gd, Sm).

6 Literature

[1] *Malavasi, L.; Fisher, C.A.J.; Islam, M.S.:* Oxide-ion and proton conducting electrolyte materials for clean energy applications: structural and mechanistic features. *In:* Chemical Society reviews, Vol. 39 (2010), Iss. 11, pp. 4370-4387.

[2] *Dubois, A.; Ricote, S.; Braun, R.J.:* Benchmarking the expected stack manufacturing cost of next generation, intermediate-temperature protonic ceramic fuel cells with solid oxide fuel cell technology. *In:* Journal of Power Sources 369 (2017), S. 65-77.

[3] *Choi, S.; Kucharczyk, C.J.; Liang, Y. et al.:* Exceptional power density and stability at intermediate temperatures in protonic ceramic fuel cells. *In:* Nature Energy 3 (2018), Heft 3, S. 202-210.

[4] *Duan, C.; Tong, J.; Shang, M. et al.:* Readily processed protonic ceramic fuel cells with high performance at low temperature. *In:* Science, Vol. 349 (2015), Iss. 6254, pp. 1321-1326.

[5] *Larminie, J.; Dicks, A.:* Fuel cell systems explained. J. Wiley, Chichester, West Sussex, 2011.

[6] *Shao, Z.; Tadé, M.O.:* Intermediate-Temperature Solid Oxide Fuel Cells. Springer Berlin Heidelberg, Berlin, Heidelberg, 2016.

[7] *An, H.; Lee, H.-W.; Kim, B.-K. et al.:* A 5×5 cm^2 protonic ceramic fuel cell with a power density of 1.3 W cm^{-2} at 600 °C. *In:* Nature Energy 3 (2018), Heft 10, S. 870-875.

[8] *Kreuer, K.D.;* St. Adams*; Münch, W. et al.:* Proton conducting alkaline earth zirconates and titanates for high drain electrochemical applications. *In:* Solid State Ionics 145 (2001), S. 295-306.

[9] *Duan, C.; Tong, J.; Shang, M. et al.:* Supplementary: Readily processed protonic ceramic fuel cells with high performance at low temperature. *In:* Science (New York, N.Y.), Vol. 349 (2015), Iss. 6254, pp. 1321-1326.

[10] *Iwahara, H.; Esaka, T.; Uchida, H. et al.:* Proton conduction in sintered oxides and its application to steam electrolysis for hydrogen production. *In:* Solid State Ionics (1981), Heft 3, S. 359-363.

[11] *Zohourian, R.; Merkle, R.; Raimondi, G. et al.:* Mixed-Conducting Perovskites as Cathode Materials for Protonic Ceramic Fuel Cells: Understanding the Trends in Proton Uptake. *In:* Advanced Functional Materials 28 (2018), Heft 35, S. 1801241.

[12] *Iwahara, H.:* Proton conducting ceramics and their applications. *In:* Solid State Ionics 86-88 (1996), S. 9-15.

[13] *Merkle, R.; Zohourian, R.; Maier, J.:* Two-fold stoichiometry relaxation — Simulated relaxation kinetics of ionic and electronic defect concentrations. *In:* Solid State Ionics 288 (2016), S. 291-297.

[14] *Wang, H.; Wang, X.; Meng, B. et al.:* Perovskite-based mixed protonic–electronic conducting membranes for hydrogen separation: Recent status and advances. *In:* Journal of Industrial and Engineering Chemistry 60 (2018), S. 297-306.

[15] *Hyun Ryu, K.; Haile, S.M.:* Chemical stability and proton conductivity of doped $BaCeO_3$ – $BaZrO_3$ solid solutions. *In:* Solid State Ionics 125 (1999), S. 355-367.

[16] *Rosensteel, W.A.; Ricote, S.; Sullivan, N.P.:* Hydrogen permeation through dense $BaCe_{0.8}Y_{0.2}O_{3-\delta}$ – $Ce_{0.8}Y_{0.2}O_{2-\delta}$ composite-ceramic hydrogen separation membranes. *In:* International Journal of Hydrogen Energy 41 (2016), Heft 4, S. 2598-2606.

[17] *Zhao, Z.; Cui, J.; Zou, M. et al.:* Novel twin-perovskite nanocomposite of Ba–Ce–Fe–Co–O as a promising triple conducting cathode material for protonic ceramic fuel cells. *In:* Journal of Power Sources 450 (2020), S. 227609.

[18] *Cheng, S.; Wang, Y.; Zhuang, L. et al.:* A Dual-Phase Ceramic Membrane with Extremely High H_2 Permeation Flux Prepared by Autoseparation of a Ceramic Precursor. *In:* Angewandte Chemie (International ed. in English), Vol. 55 (2016), Iss. 36, pp. 10895-10898.

[19] *Cheng, S.; Wang, Y.; Zhuang, L. et al.:* Supplementary: A Dual-Phase Ceramic Membrane with Extremely High H_2 Permeation Flux Prepared by Autoseparation of a Ceramic Precursor. *In:* Angewandte Chemie (International ed. in English) 55 (2016), Heft 36.

[20] *Shannon, R.D.:* Revised Effective Ionic Radii and Systematic Studies of Interatomie Distances in Halides and Chaleogenides. *In:* Acta Cryst. (1976), A32, S. 751-767.

[21] *Ishihara, T.:* Perovskite Oxide for Solid Oxide Fuel Cells. Springer US, Boston, MA, 2009.

[22] *Sgourou, E.N.; Panayiotatos, Y.; Davazoglou, K. et al.:* Self-Diffusion in Perovskite and Perovskite Related Oxides: Insights from Modelling. *In:* Applied Sciences 10 (2020), Heft 7, S. 2286.

[23] *Zhang, H.; Wilhite, B.A.:* Electrical conduction and hydrogen permeation investigation on iron-doped barium zirconate membrane. *In:* Journal of Membrane Science 512 (2016), S. 104-110.

[24] *Duan, C.; Huang, J.; Sullivan, N. et al.:* Proton-conducting oxides for energy conversion and storage. *In:* Applied Physics Reviews 7 (2020), Heft 1, S. 11314.

[25] *Liu, Y.; Ran, R.; Tade, M.O. et al.:* Structure, sinterability, chemical stability and conductivity of proton-conducting $BaZr_{0.6}M_{0.2}Y_{0.2}O_{3-\delta}$ electrolyte membranes: The effect of the M dopant. *In:* Journal of Membrane Science 467 (2014), S. 100-108.

[26] *Livage, J.; Henry, M.; Sanchez, C.:* Sol-gel chemistry of transition metal oxides. *In:* Prog. Solid St. Chem. (1988), Heft 18, S. 259-341.

[27] *Pillai, S.C.; Hehir, S.:* Sol-Gel Materials for Energy, Environment and Electronic Applications. Springer International Publishing, Cham, 2017.

[28] *Van der Pauw, L.J.:* A method of measuring specific resistivity and hall effect of discs of arbitrary shape. *In:* Philips Research Reports 13 (1958), Heft 1, S. 1-9.

[29] Van-der-Pauw-Messmethode, „https://de.wikipedia.org/w/index.php?title=Van-der-Pauw-Messmethode&oldid=201616788" [Zugriff am: 23.03.2021].

[30] *Van der Pauw, L.J.:* A method of measuring the resistivity and hall coefficient on lamellae of arbitrary shape. *In:* Philips Technical Review 20 (1958/59), Heft 8, S. 220-224.

[31] *Preis, W.; Bucher, E.; Sitte, W.:* Oxygen exchange measurements on perovskites as cathode materials for solid oxide fuel cells. *In:* Journal of Power Sources 106 (2002), S. 116-121.

[32] *Lane, J.A.; Kilner, J.A.:* Measuring oxygen diffusion and oxygen surface exchange by conductivity relaxation. *In:* Solid State Ionics (2000), 136-137, S. 997-1001.

[33] *Berger, C.:* Development of new materials for solid oxide fuel cell cathodes with superior performance and improved long-term stability, Doctoral Thesis.

[34] *Berger, C.; Bucher, E.; Sitte, W.:* Mass and charge transport properties of $La_{0.9}Ca_{0.1}FeO_{3-\delta}$. *In:* Solid State Ionics 299 (2017), S. 46-54.

[35] *Schrödl, N.; Bucher, E.; Egger, A. et al.:* Long-term stability of the IT-SOFC cathode materials $La_{0.6}Sr_{0.4}CoO_{3-\delta}$ and $La_2NiO_{4+\delta}$ against combined chromium and silicon poisoning. *In:* Solid State Ionics 276 (2015), S. 62-71.

[36] *Preis, W.; Bucher, E.; Sitte, W.:* Oxygen exchange kinetics of $La_{0.4}Sr_{0.6}FeO_3$ by simultaneous application of conductivity relaxation and carrier gas coulometry. *In:* Solid State Ionics 175 (2004), 1-4, S. 393-397.

[37] *Hombo, J.; Matsumoto, Y.; Kawano, T.:* Electrical Conductivities of $SrFeO_{3-\delta}$ and $BaFeO_{3-\delta}$ Perovskites. *In:* Journal of Solid State Chemistry 84 (1990), S. 138-143.

[38] *Pulphol, P.; Vittayakorn, N.; Vittayakorn, W. et al.:* Electrical conductivity, magnetism, and optical properties of reduced $BaCeO_3$. *In:* Applied Physics A 125 (2019), Heft 197.

[39] *Triviño-Peláez, Á.; Pérez-Coll, D.; Mather, G.C.:* Electrical properties of proton-conducting $BaCe_{0.8}Y_{0.2}O_{3-\delta}$ and the effects of bromine addition. *In:* Acta Materialia 167 (2019), S. 12-22.

[40] *Zohourian, R.:* Mixed-conducting perovskites as cathodes in protonic ceramic fuel cells: Defect chemistry and transport properties.

[41] *Egger, A.; Bucher, E.; Yang, M. et al.:* Comparison of oxygen exchange kinetics of the IT-SOFC cathode materials $La_{0.5}Sr_{0.5}CoO_{3-\delta}$ and $La_{0.6}Sr_{0.4}CoO_{3-\delta}$. *In:* Solid State Ionics 225 (2012), S. 55-60.

[42] *Bucher, E.; Egger, A.; Ried, P. et al.:* Oxygen nonstoichiometry and exchange kinetics of $Ba_{0.5}Sr_{0.5}Co_{0.8}Fe_{0.2}O_{3-\delta}$. *In:* Solid State Ionics 179 (2008), 21-26, S. 1032-1035.

7 List of figures

8 List of tables

9   List of equations

10 Appendix

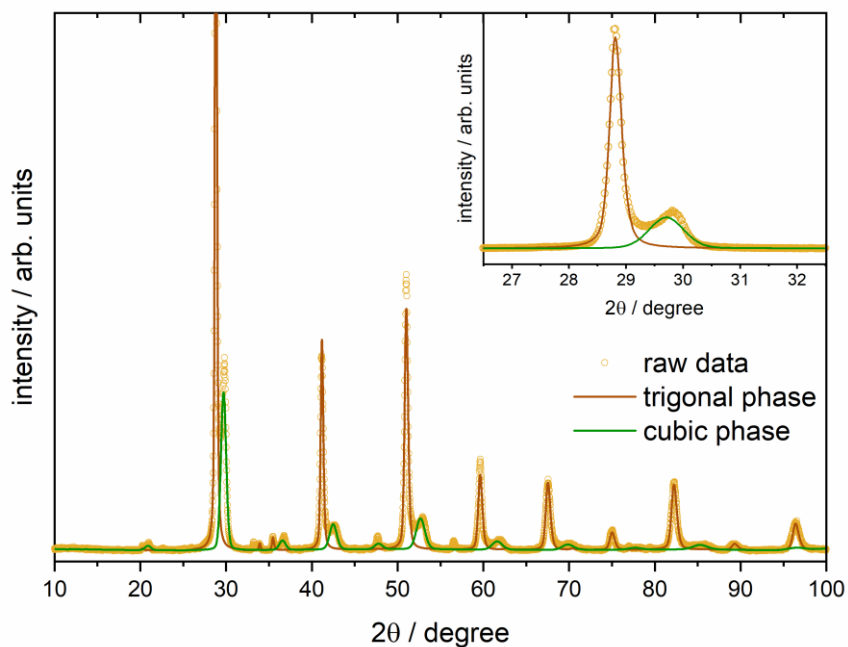## 10.1 Powder diffraction patterns

10.1.1 BCFY622

Figure 42 | Powder diffraction pattern (circles) and Rietveld refinement (solid line) of BCFY622
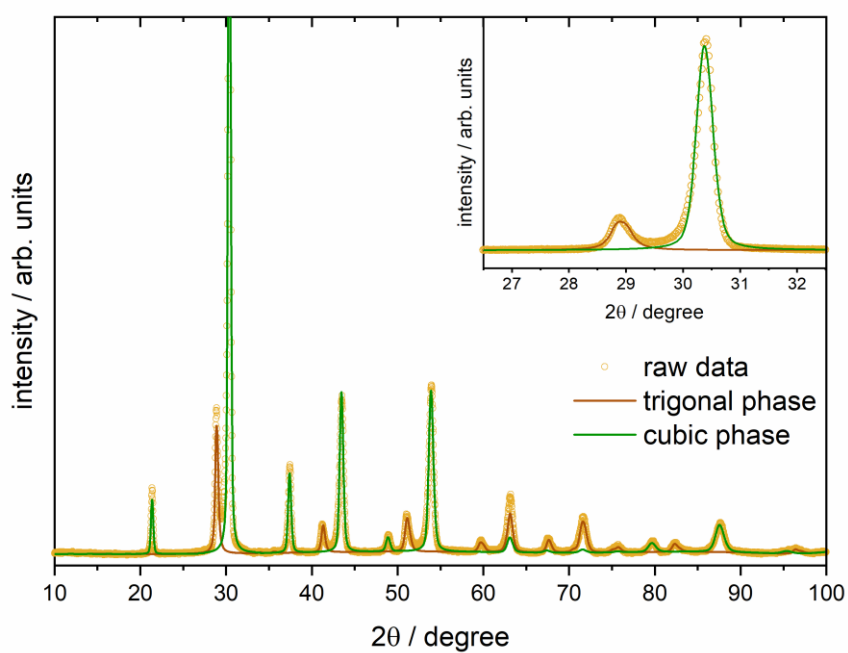
10.1.2 BCFY262

Figure 43 | Powder diffraction pattern (circles) and Rietveld refinement (solid line) of BCFY262

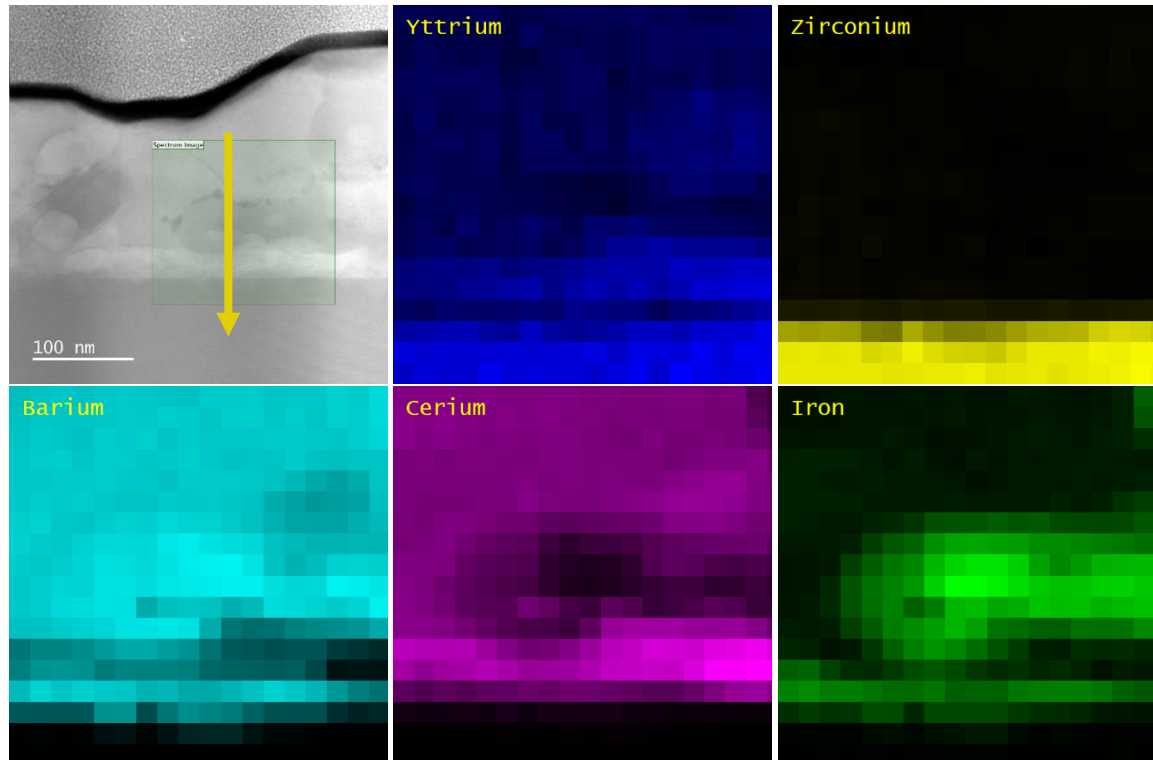## 10.2 Transmission electron microscopy

10.2.1 BCFY622

Figure 44 | STEM-EDX elemental maps of Ba, Fe, Ce, Y and Zr in the composite BCFY622 (thin film on YSZ substrate)
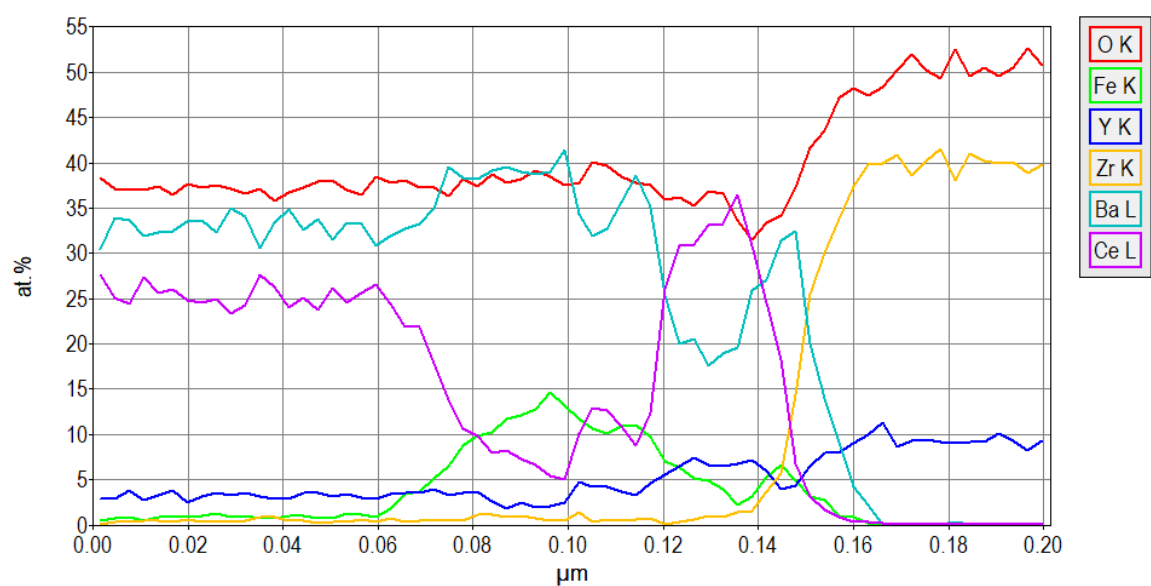
Figure 45 | EDX profile over the area marked in yellow in Figure 44
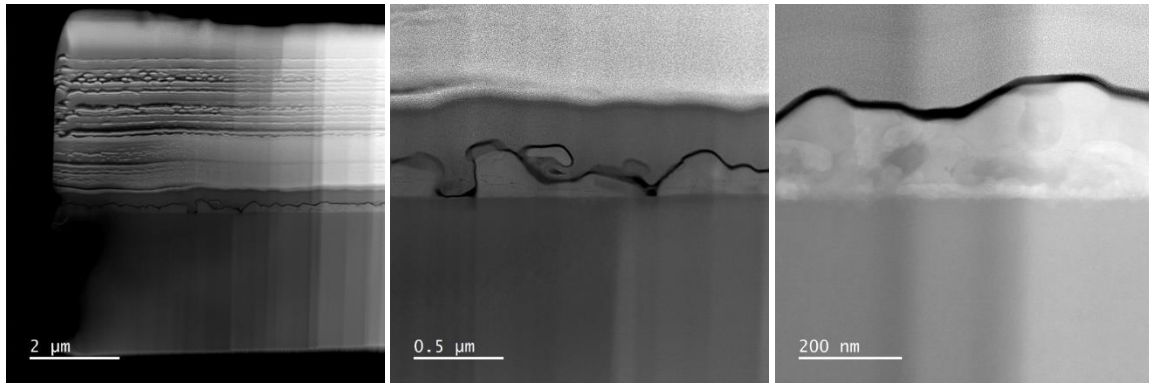
Figure 46 | STEM-HAADF images of a thin-film of BCFY622 on YSZ

10.2.2 BCFY262
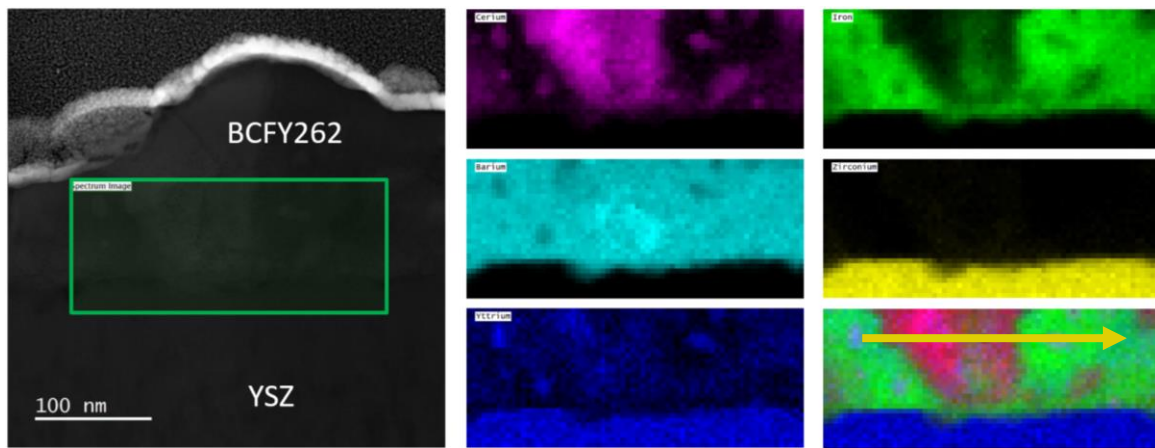
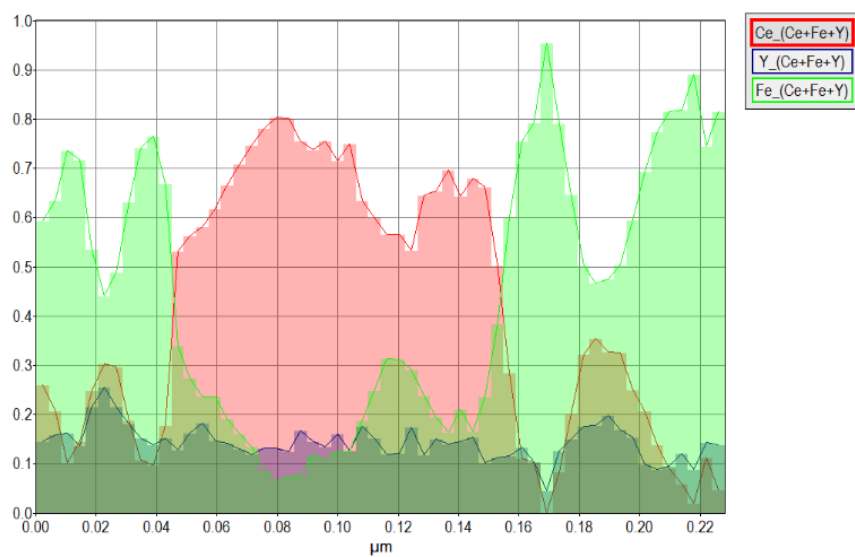*Figure 47 | STEM-EDX elemental maps of Ba, Fe, Ce, Y and Zr in the composite BCFY262 (thin film on YSZ substrate)*

Figure 48 | EDX profile over the area marked in yellow in Figure 47
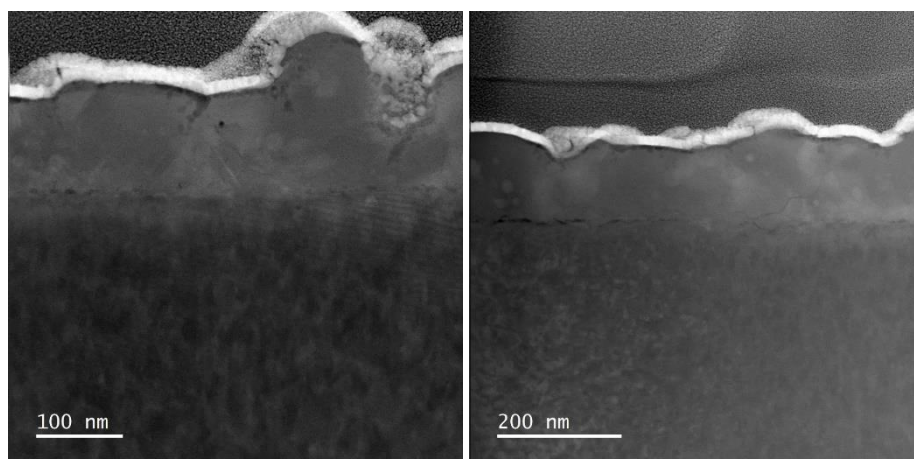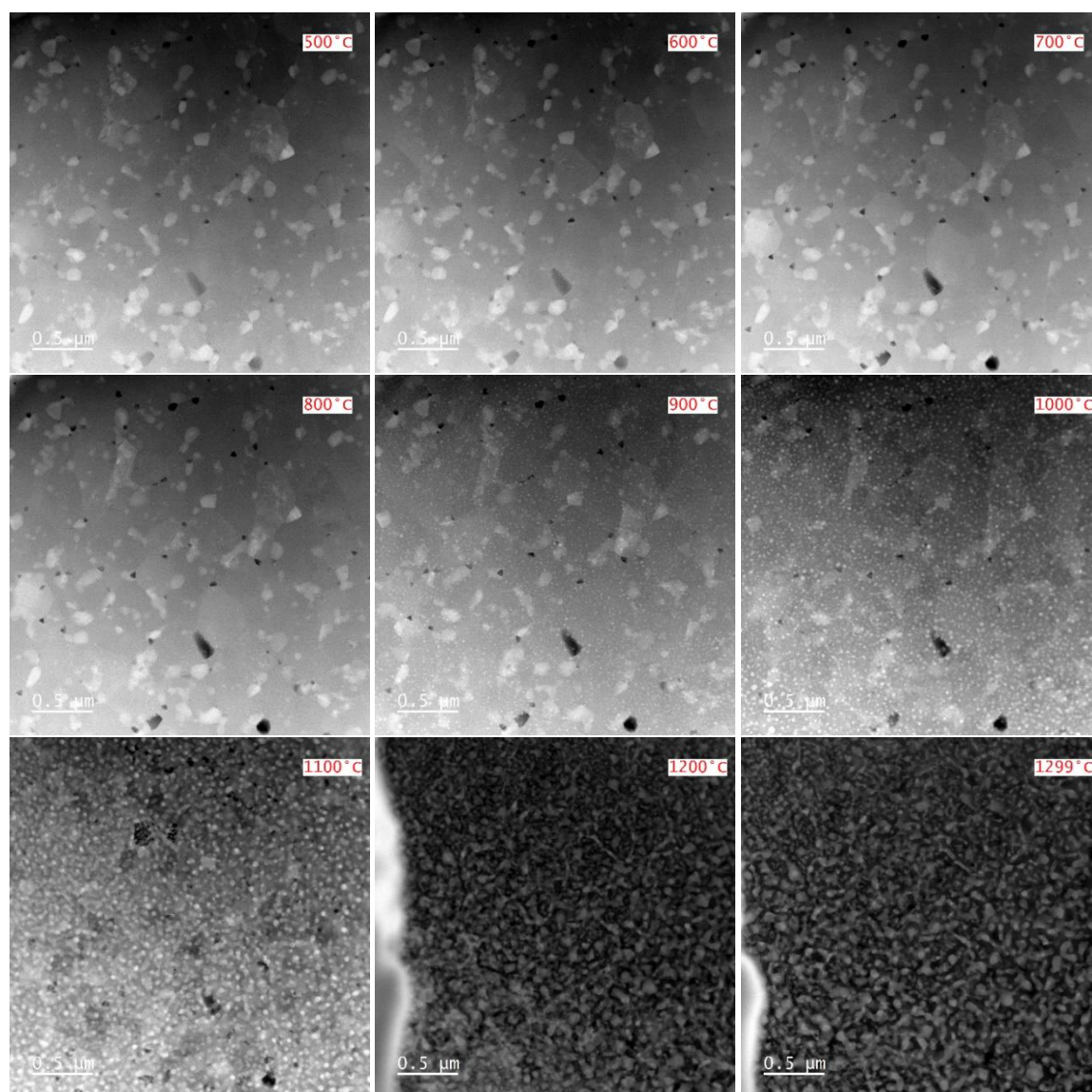
Figure 49 | STEM-HAADF images of a thin-film of BCFY262 on YSZ

Figure 50 | Images of the in-situ TEM heating experiment of BCFY262
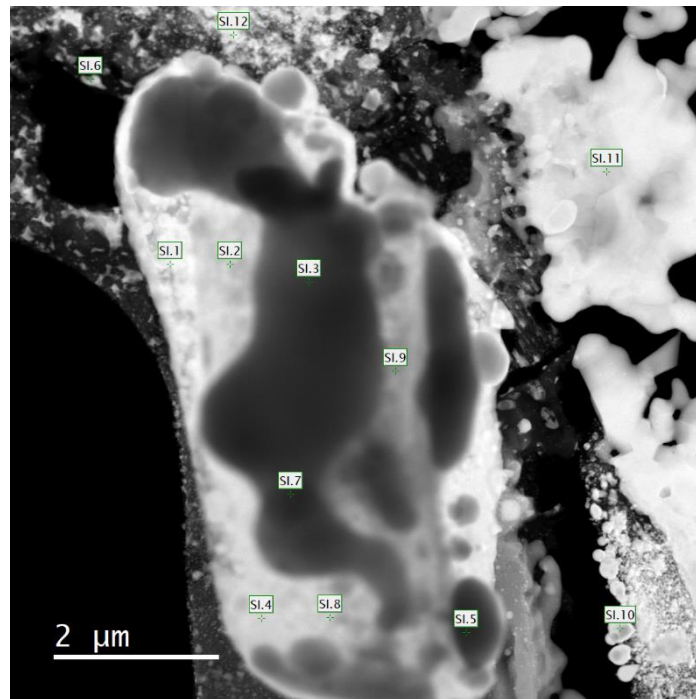
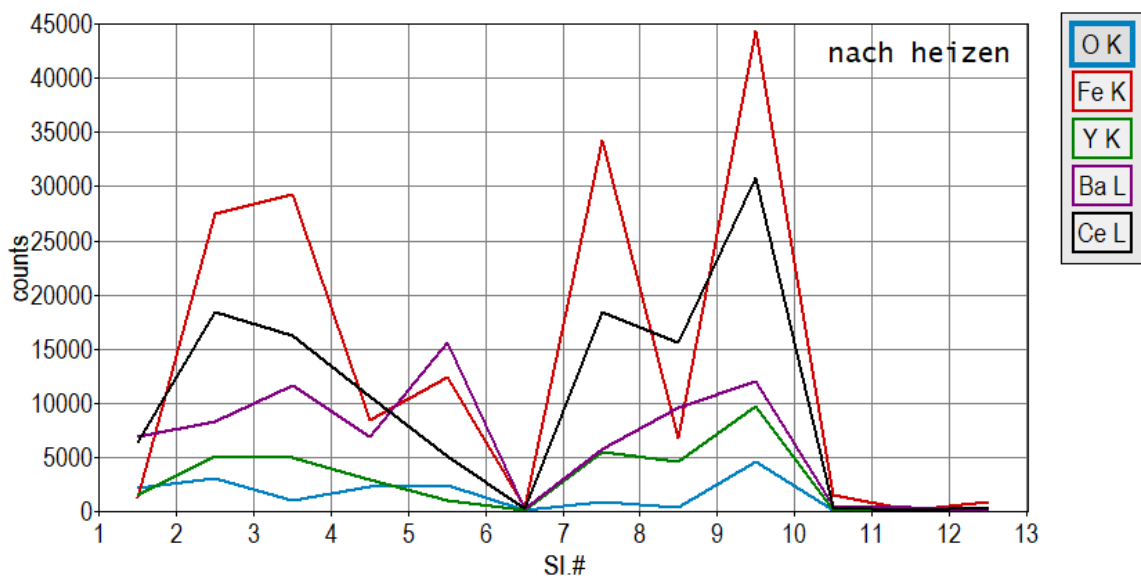*Figure 51 | BCFY262 after the heating experiment*

Figure 52 | EDX point spectra of BCFY262 (points marked in Figure 51)